Final Technical Report - DE-FG02-07ER15901 - Reaction mechanisms for barite dissolution and growth. **PI** - Andrew G. Stack

BES grant DE-FG02-07ER15901 ($209,747; 09/01/07 - 08/31/09, extended to 04/01/10) funded the publication of three manuscripts published in peer-reviewed journals (Stack and Rustad, 2007; Stack, 2009; Wang et al., 2010), one that is in preparation (Wang and Stack, in prep.) and produced data for a future manuscript (Stack et al., planned). The focus of the work was measurement and simulation of the rates of processes occurring at aqueous-crystalline interfaces, particularly the mineral barite ($BaSO_4$). In addition to supporting the PI, the work supported one post-doctoral researcher (Xuefeng Wang), a semester-long research project of an undergraduate student (Jacquelyn Bracco), and materials and supplies for the work as well as travel to professional society meetings (American Chemical Society; Geochemical Society).

In Stack and Rustad (2007), the reactive flux method (Rey and Hynes, 1996) and molecular dynamics (MD) were used to simulate the {001} barite-water interface structure and water exchange rate of aqueous barium ions and barium surface species. Atomic-level mineral-water interfacial structure and kinetics are being studied with increasing precision due to advances in spectroscopic methods at synchrotron x-ray sources as well as improved computational capacity. Better characterization of these interfaces in turn is leading to advances in the understanding of many macroscopic geochemical properties. Overall the barite-water interfacial structure was found to compare well to that estimated using X-ray reflectivity (XRR) measurements (Fenter et al., 2001), but there was an important difference: the MD predicted an intricate water structure present at the interface with one major peak and several minor peaks whereas the XRR found only a single layer of water. This discrepancy is thought to result from a limited resolution in the Fenter et al. (2001) study as well as over-coordination of surface sulfates by the MD model.

The water exchange rates of the aqueous barium ion was successfully simulated at $k = 4.8 \times 10^9$ s^{-1} in this manuscript with 20-30% variability in rate constant depending on transition state choice. This estimate falls within the range of earlier estimates of 10^9-10^{10} s^{-1} (Richens, 1997). The calculated water-exchange rate of barium ions at the barite-water interface was found to be 3.5 times faster, which contrasts to previous estimates of water exchange on calcium ions on calcite surfaces (Kerisit et al., 2004), but is consistent with the behavior of aluminum ions on a variety of minerals (Wang et al., 2007). At this point, it is not clear if the difference in relative exchange rates is intrinsic to the identity of the ion or mineral, or an artifact caused by simulation details. This manuscript was an achievement not only because we successfully predicted the rate of an important geochemical reaction, but because it remains the only sensitivity analysis of rates estimated using the reactive flux method.

In Stack (2009), the PI adjusted the MD force field in Stack and Rustad (2007) to better model the aqueous ion hydration enthalpies. Using this improved force field, the PI examined the enthalpies of kink site formation on barite [120] steps, an intrinsic property of a mineral that determines growth and dissolution kinetics. The calculated enthalpies of attachment and detachment for ten different surface sites along a step edge were compared to the experimental estimate made by Higgins et al. (2000). It was found that it was not possible to relate the kink site formation enthalpy of any single reaction to the experimental estimate. This suggests that the mechanism(s) of growth and dissolution are more complicated than simple attachment or detachment at step edges and kink sites. After taking the average over all sites and treating the attachment enthalpies as minimum estimates of the activation energy, it was found that the

apparent kink site formation energy was of similar magnitude to the experimental estimate, but the wrong sign. The reason for the discrepancy is not known. Additionally, the coordination number to water of surface barium ions was examined. It was found that the number of water molecules coordinating a surface barium ion was nearly always under-coordinated relative to the proportional number of oxygens on sulfate. If the assumption of a direct proportionality between coordination by sulfate and coordination by water for various surface states is valid, it suggests that there is a steric hindrance presented by the interface that hinders water adsorption to surface sites. No other data exists on the sterics of solvation at this interface.

Wang et al. (2010) and Wang and Stack (in prep.) deal with nucleation rate and growth morphology of materials on functionalized self-assembled monolayers (SAMs) that mimic biological membranes. This rationale for this work is that a variety of biomineralization processes take place on biological membranes, but this could also be important in the design of new materials who are engineered or tailored to display a specific physical property. In Wang et al. (2010), the nucleation of hematin on SAMs terminated with carbonyl, hydroxyl, amine and methyl groups was monitored as a function of time and the presence of a known growth inhibitor for hematin nucleation, chloroquine. This particular system is important in that the malaria parasite crystallizes the toxic heme from metabolized red blood cells and anti-malarials such as chloroquine are thought to interfere with that process, possibly through an abiotic growth inhibition reaction (thus poisoning the parasite). It was found that the identity of the terminal functional group of the SAM strongly influenced the nucleation rate of hematin in presence of the anti-malarial. Specifically, the carbonyl terminated SAM markedly enhanced the inhibition of nucleation by the choroquine. This work may have implications for our fundamental understanding of nucleation on bio-inspired surfaces and may aid in the design of new anti-malarial drugs.

In a companion manuscript to Wang et al., (2010), the same method of nucleation on SAMs was applied to the barite-water system (Wang and Stack, in prep.). Here, the system variables pH and aqueous cation-to-anion ratio were manipulated to examine how heterogeneous nucleation of barite is influenced by the protonation state of the terminal functional group of the SAMs and the rate limiting step of reaction. It was found that nucleation is enhanced under low pH conditions under which the amine group on the SAM can be expected to be protonated. This contrasts with the results on the carbonyl-terminated SAM, where nucleation was enhanced at moderate pHs. Mixtures of differently functionalized SAMs were found to enhance nucleation greatly in all cases.

Lastly, the grant produced results for a manuscript that is being planned on homogeneous barite growth as a function of aqueous cation-to-anion ratio (Stack et al., planned). The understanding of crystal growth under variable cation-to-anion ratio is important because natural environments are often non-stoichiometric for a given material. Figure 1 shows a sequence of atomic force microscope (AFM) images of a barite (001) surface under a fixed saturation index (SI = $\log(a_{Ba}{}^{*}a_{SO4}/K_{sp})$) of 1.9, but a varying ratio of barium-to-sulfate. The figure shows a series of images centered on a number of spiral hillocks, which are growth features centered around a screw dislocation. This dislocation readily generates new bilayer steps during growth and reproduces itself with each new layer. As the hillock climbs, existing layers advance and the size of the feature increases. In Figure 1, what starts as the familiar square pyramidal growth hillocks under a 1:1 ratio becomes "capped" as [Ba]/[SO_4] is increased, indicating that generation of new steps at first slows (Figure 1c) and then ceases

altogether (Figure 1d-f). What is most striking is that the island to the right of the asterisk in Figure 1e is not present in Figure 1f. The inset shows the sequence of images after the solution in Figure 1f is introduced; the island shrinks and disappears. In addition to the data in Figure 1, similar experiments were conducted where the step velocity was measured under high sulfate-to-barium conditions and activation energies were calculated for step retreat during dissolution. This manuscript should have a substantial impact on our understanding of crystal growth and dissolution under variable cation-to-anion conditions because it shows that morphology and growth rates are strongly affected by not just the supersaturation of a solution, but the cation-to-anion ratio.

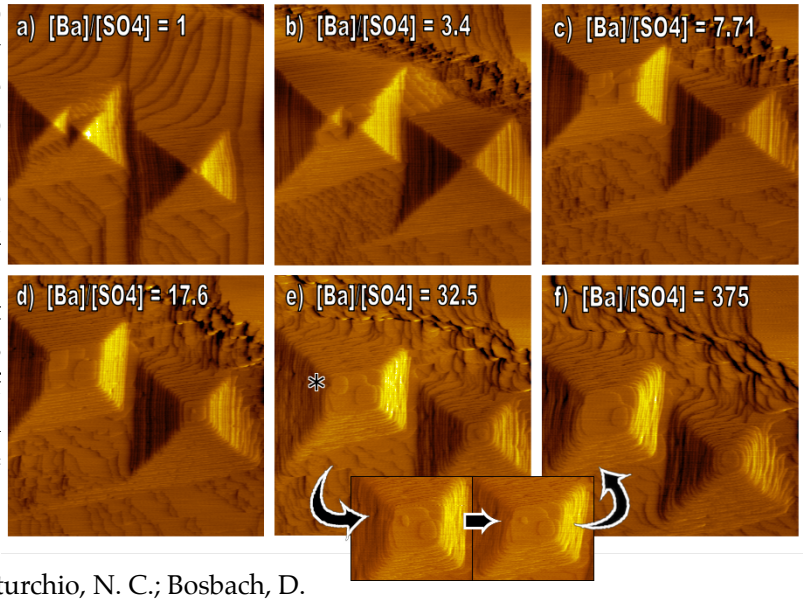

Figure 1. **a-f)** A sequence of 6 × 6 μm atomic force microscopy deflection images of the same geographical location exposed to SI = 1.9 solution but with [Ba]/[SO_4] ratios as marked. The island to the right of the asterisk is present in **a-e**, but missing in **f**, indicating dissolution. Inset shows the sequence of images demonstrating the evolution of the topography once the solution in part **f** is introduced. (Temp. = 66 °C)

References

Fenter, P.; McBride, M. T.; Srajer, G.; Sturchio, N. C.; Bosbach, D. (2001) Structure of barite (001)- and (210)-water interfaces. *J. Phys. Chem. B*, **105**, 8112-8119.

Higgins, S. R.; Bosbach, D. R.; Eggleston, C. M.; Knauss, K. G. (2000) Kink dynamics and step growth on barium sulfate (001): A hydrothermal scanning probe microscopy study. *J. Phys. Chem. B*, **104**, 6978-6982.

Kerisit, S.; Parker, S. C. (2004) Free energy of adsorption of water and metal ions on the $\{10\bar{1}4\}$ calcite surface. *J. Am. Chem. Soc.*, **126**, 10152-10161.

Rey, R.; Hynes, J. T. (1996) Hydration shell exchange kinetics: an MD study for Na^{+}_{aq}. *J. Phys. Chem.*, 1996, 5611-5615.

Richens, D. T. (1997) *The Chemistry of Aqua Ions*. Wiley & Sons, New York.

Stack, A. G.; Rustad, J. R. (2007) Structure and dynamics of water on aqueous barium ion and the {001} barite surface. *J. Phys. Chem. C*, **111**, 16387-16391.

Stack, A. G. (2009) Molecular dynamics simulations of solvation and kink site formation at the {001} barite-water interface. *J. Phys. Chem. C*, **113**, 2104-2110.

Stack, A. G.; Wang, X.; Bracco, J.; Grantham, M. C. (planned) Growth and dissolution of barite [120] steps: experimental, theoretical and computational perspectives.

Wang, J.; Rustad, J. R.; Casey, W. H. (2007) Calculation of water-exchange rates on aqueous polynuclear clusters and at oxide-water interfaces. *Inorg. Chem.*, **46**, 29620-2964.

Wang, X.; Stack, A. G. (in prep.) The role of pH and terminal moiety in barite nucleation on self-assembled monolayers.

Wang, X.; Ingall, E.; Lai, B.; Stack, A. G. (2010) Self-assembled monolayers as templates for heme crystallization. *Cryst. Growth Des.*, **10**, 798-805.

Structure and Dynamics of Water on Aqueous Barium Ion and the {001} Barite Surface

Andrew G. Stack*,† and James R. Rustad‡

School of Earth and Atmospheric Sciences, Georgia Institute of Technology, 311 Ferst Drive, Atlanta, Georgia 30332, and Department of Geology, University of California, Davis, One Shields Avenue, Davis, California 95616

Received: June 18, 2007; In Final Form: August 16, 2007

The structure of water and its dynamics affect a number of fundamental properties of an interface. Yet, these properties are often inaccessible experimentally and computational studies including solvent are comparatively few. Here, we estimate the structure and kinetics of water exchange of aqueous barium ions and barium ions within the {001} barite surface using molecular dynamics and the reactive flux method. For the aqueous ion, the Ba−O distance to water in the first hydration shell was found to be 280 pm with a coordination number of 8.3, and the best estimate of the exchange rate constant is 4.8×10^9 s^{-1}, closely matching experimental estimates. For the barite surface, the first shell water distance was 282 pm, with a coordination number of 0.9 and the best estimate of the rate constant for exchange is 1.7×10^{10} s^{-1}, 3.5 times faster than that of the aqueous ion.

Introduction

Water structure and exchange rate are fundamental properties of aqueous ions and solid−water interfaces and play an important role in a number of surface processes such as growth, dissolution, adsorption, desorption, etc. For example, the dissolution rate of isostructural crystalline materials with variation in the identity of the cation often correlates to the water exchange rate of the aqueous form of the cation.[1−3] While experimental measurements have given some indication of water exchange at mineral−water interfaces,[4] the water exchange rates of specific surface species are often ambiguous due to high variability in surface structure and morphology within a single sample preparation. Computational techniques are now sufficiently advanced to precisely calculate the rate of water exchange on surfaces and possibly model limiting reactions.

The goals of the present molecular dynamics (MD) study are twofold: (1) to estimate the water structure on the {001} barite surface and (2) to estimate the rate of exchange on an aqueous barium ion and barium ions embedded in the {001} surface of barite (barium sulfate), using the reactive flux method. The interface structure is compared to a fit of X-ray Reflectivity (XRR) experiments.[5,6] The MD force field and methods are calibrated on aqueous barium ion, whose water exchange rate is too fast to be precisely resolved by using NMR methods, but is in the range of 10^9-10^{10} s^{-1}.[7−9] Reactive flux has been used previously to calculate water exchange rates of the aqueous ions Li^+,[10−12] Na^+,[13] as well as aluminum polyoxometalates, oxyhydroxides, and aluminum silicates,[14] aqueous calcium, magnesium, and strontium ions, and calcite mineral surfaces.[15]

Barite was chosen because it is commonly used industrially as a weighting agent to increase the density of drilling fluid. Its precipitation as scale can sometimes completely inhibit oil recovery in reservoirs where high sulfate seawater mixes with host rock with significant barium (or strontium). In natural environments, barite is found suspended in the upper water column in oceans and in sediments, yet these waters are usually undersaturated with respect to barite.[16] Its accumulation in sediments is used as a biomarker indicating high biological primary productivity.[17] Finally, it is a biomineral, directly precipitated by some benthic and freshwater organisms including species of foraminifera and algae[18] and indirectly precipitated onto diatoms.[19]

Methods

In the reactive flux method, the overall rate constant for the exchange, k, is the product of the transition state theory rate constant, k_{TST}, and the transmission coefficient, κ: $k = \kappa k_{TST}$. k_{TST} is expressed in terms of the reaction coordinate, ξ:

$$k_{TST} = \frac{\langle|\dot{\xi}|\rangle_{\xi^\ddagger}}{2} \frac{P(\xi^\ddagger)}{\int_{-\infty}^{\xi^\ddagger} P(\xi)\, d\xi} \quad (1)$$

where $\dot{\xi}$ is the velocity with respect to the reaction coordinate, $\xi^\ddagger$ is the transition state, $P(\xi^\ddagger)$ is a probability distribution function, and $\langle ... \rangle$ denotes an average.[20−22] The value of k_{TST} is dependent on the choice of transition state location and the reaction coordinate definition.[20] For water exchange reactions on an aqueous ion, ξ is typically defined as the distance r between the ion and the exchanging water and k_{TST} is calculated from the potential of mean force, $W(r)$, between the ion and water at distance r:

$$k_{TST} = \sqrt{\frac{1}{2\pi\beta\mu}} \frac{r^{\ddagger 2} e^{-\beta W(r^\ddagger)}}{\int_0^{r^\ddagger} r^2 e^{-\beta W(r)}\, dr} \quad (2)$$

where $\beta = 1/k_b T$, μ is the ion−water pair reduced mass, and $r^\ddagger$ is the distance at which $W(r)$ is a maximum, i.e., the transition state.[10,13] For fast reactions, $W(r)$ is typically estimated from the radial distribution function, $g(r)$: $W(r) = -\beta^{-1} \ln(g(r))$, which is sufficient to provide adequate sampling of the transition state.

* Address correspondence to this author. E-mail: andrew.stack@eas.gatech.edu.
† Georgia Institute of Technology.
‡ University of California, Davis.

10.1021/jp0747196 CCC: $37.00
Published on Web 10/18/2007

The transition state is used as a starting structure to estimate a time-dependent transmission coefficient, $\kappa(t)$:

$$\kappa(t) = \frac{\langle \delta[\xi(0) - \xi^{\ddagger}]\dot{\xi}(0)\theta[\xi(t) - \xi^{\ddagger}]\rangle}{\langle \delta[\xi(0) - \xi^{\ddagger}]\dot{\xi}(0)\theta[\dot{\xi}(0)]\rangle} \quad (3)$$

where $\xi(t)$ is the reaction coordinate at time t, θ is the Heaviside step function, and δ is the derivative of θ. The numerator is averaged over all configurations that start from the transition state and are in a product state at time t later, weighted by the velocity with respect to the reaction coordinate. The denominator is the average velocity with respect to the reaction coordinate of all the configurations that start from the transition state with a positive velocity. Similar to eq 2, the ion−oxygen on water distance is used as the reaction coordinate for water exchange on aqueous ions. Once the overall rate constant, k, has been calculated, the mean residence time, τ, of water in the first shell can be calculated by taking the reciprocal of k.

The force field used here with slight modification was developed by Jang et al.[23] It is based on the DREIDING formulism[24] and the F3C flexible water model.[25] Although multiple barite MD force fields exist,[26,27] this particular force field was chosen because it had been tested against the vibrational frequencies of sulfate as well as including Van der Waals interactions on the protons on the water, which may be important to consider for interaction with mineral surfaces. The force field was adapted to the LAMMPS software package[28] and validated by comparing the results for the bulk water and barite to those of Jang et al.[23] All calculations were performed in the canonical (NVT) ensemble, a time step (ts) of 1 fs, a standard Ewald summation (tolerance = 5e−5; cutoff = 6 Å), a velocity-Verlet time integration,[29] and a Nosé−Hoover thermostat.[30−32] For aqueous ions, a 20 × 20 × 20 Å^3 periodic cell was used with 267 water molecules and one ion. For the {001} barite surface, two supercells were used. For the kinetics, the supercell was 26.65 × 21.82 × 42.94 Å^3. This cell included 144 formula units of $BaSO_4$, within 6 monolayers (half of the z dimension), and 416 water molecules. A larger supercell was used, 34.45 × 28.14 × 57.26 Å^3, in order to achieve more bulk-like water and barite for comparison to the XRR.

The $W(r)$ was calculated by using the average $g(r)$ at (0.6 pm bin size) from a 10 ns simulation (10^7 time steps). The {001} surface of barite includes two types of surface barium ions in the first monolayer, but we only estimate the kinetics and structure on the topmost site, closest to the water. To generate the initial configurations for the transmission coefficient, a 10 ns simulation was conducted with a water molecule constrained at $r^{\ddagger}$ distance from the ion, using the SHAKE algorithm.[33] Positions and velocities were harvested from the second half of this simulation every 5000 ts, or 5 ps, generating 1001 configurations. κ was calculated from the average plateau value of 2 ps simulations of these trajectories, run forward and backward in time, with random velocities assigned to both the ion and the formerly constrained water molecule.

Results and Discussion

Structure and Hydration Energy. Jang et al.[23] did a substantial evaluation of the bulk and interfacial barite and Levitt et al.[25] examined bulk water, thus we will only dwell on those characterizations here enough to demonstrate the applicability of our implementation. The potential energy of bulk barite was calculated here at −2480 kJ/mol, which compares favorably to the Jang et al.[23] result (−2461 kJ/mol) and their estimate of the lattice energy from hydration enthalpies (−2478 kJ/mol). The potential energy of bulk water is calculated here to be −42 kJ/mol, whereas the experimental measurement is −41.5 kJ/mol.[34] In our implementation of the F3C water, the OO radial distribution function ($g(r)$) maximum occurs at 273 pm with $g(r) = 3.25$, whereas the experimental estimate from neutron scattering is at 288 pm with $g(r) = 3.09$.[35] For reference, the $g(r)$ of the SPC/E model gives a mean first shell water distance of 275 pm and a height of 3.05.[36,37]

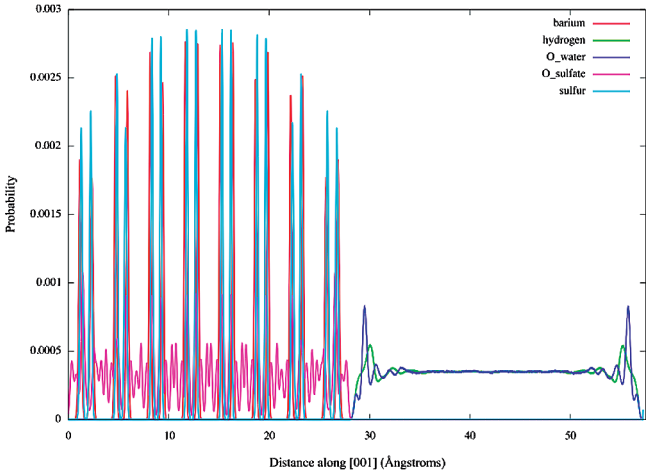

Figure 1. Normalized histogram of a barite {001} surface exposed to water. The oxygen structure shows a total of five separate peaks on water at the interface.

For an aqueous barium ion, the model gives a hydration energy of −1150 kJ/mol, a 12% error from the experimental estimate of −1305 kJ/mol.[38] The calculated Ba−O_{water} $g(r)$ peak is at 280 pm, which is in good agreement with the experimental estimate of 282(2) pm (estimated by EXAFS)[38] and a QM/MM MD estimate of 286 pm.[7] The average coordination number obtained is 8.3, similar to the estimate by EXAFS, 8.1(3).[38] However, some X-ray or NMR techniques indicate a higher coordination number of 9.5−9.7 and a QM/MM study found 9.3.[7,8] Aqueous sulfate ion coordination and structure are less well constrained experimentally, but our estimate of the mean S−O_{water} distance is 385 pm, which falls in the range of previous computational and experimental estimates, 370−390 pm.[39,40] The predicted hydration energy is −1020 kJ/mol, with a 9% difference from the experimental estimate, −1108 kJ/mol.[41] Overall we believe our implementation of this model to be fairly good at estimating the structure while retaining an acceptable accuracy in the hydration energy of the aqueous ions.

The structure of the {001} barite−water interface has been examined experimentally with use of high-resolution X-ray reflectivity (XRR) in one dimension.[5,6] While the features of the surface barium and sulfur peaks resemble that derived from the XRR data, the oxygen profiles are substantially different. The XRR data were fit by using a single adsorbed water layer with a surface barium-to-oxygen (on water) distance of 235 ± 13 pm in one dimension parallel to [001]. This is somewhat inconsistent with the results we obtain from the molecular dynamics simulations (Figure 1) where many distinct interfacial O_{water} peaks are observed. The closest (small) peak to the interface represents waters associated with the second layer of surface barium ions and is at 175 pm from the topmost layer of barium atoms, parallel to [001]. The second tallest oxygen peak represents water associated with the topmost layer of barium atoms as well as those interacting with sulfates. It is located 265 pm from the topmost layer of barium. If these two peaks are weighted by their intensity, the average height is nominally consistent with the XRR peak position within error. Furthermore,

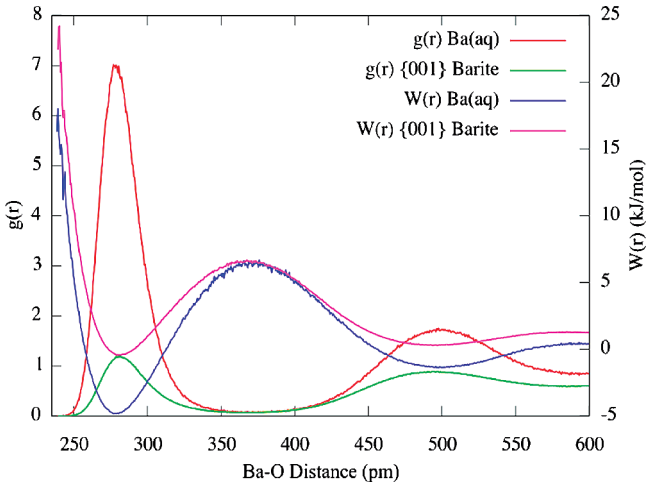

Figure 2. Ba-oxygen on water radial distribution functions, $g(r)$, and potentials of mean force, $W(r)$, for aqueous barium ion and barium ions within the {001} barite surface.

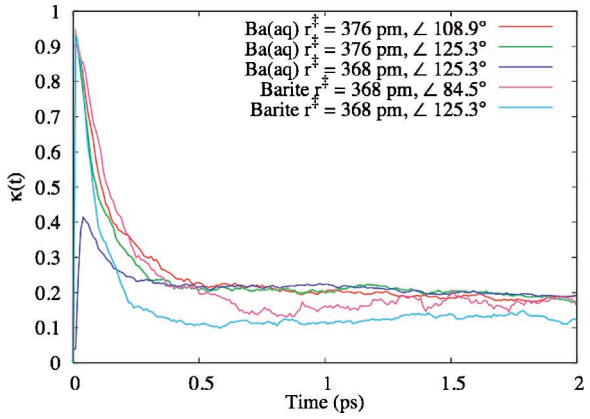

Figure 3. Time-dependent transmission coefficient, $\kappa(t)$, for aqueous barium ion and barium ions within the {001} barite surface for the best fit and sensitivity analyses (Table 1). Fits of $\kappa(t)$ were made over the range 0.5−2 ps.

if the two oxygen-on-water peaks in Figure 1 closest to the interface are integrated, the result is 2.9 oxygens per surface unit cell, encouragingly similar to the Fenter et al. estimate of 2.7 ± 0.1.[5,6]

The radial distribution function of surface bariums shows that the absolute distance to first shell water is 282 pm, very similar to that of the aqueous ion (Figure 2). The coordination number of the topmost surface bariums is 0.9, slightly less than one water molecule in contact with each surface barium on average. The range of coordination numbers observed was 0−2. The average coordination number is consistent with the XRR fit, but the XRR fit represents the total amount of water at the interface whereas in the MD simulation water was found coordinated to surface sulfates as well as bariums.

An intricate oxygen structure is also apparent in the results of previous workers,[26] although the relative magnitudes of the peaks vary. Additionally, both MD simulations show an intricate structure of the oxygens on sulfates in between monolayers. These are missing in the XRR best-fit structure. At this point, it is not clear why there is a difference between the structures of oxygen peaks in the experimental and computational profiles. On one hand, the MD simulations may be giving incorrect structures. On the other, the XRR data are derived from a structure where a single monolayer of water was assumed, but sufficiently explained the experimental data once the fit was optimized. To a certain extent, in fitting XRR reflectivity data, it is difficult to distinguish between a large broad peak and two relatively small ones (Paul Fenter, personal communication). Finally, the time scale of the MD simulation (10 ns) is presumably much shorter than that of the XRR experiment, so the XRR data may represent an average water structure that includes surface structures unaccounted for in the MD simulations. These structures include steps, adsorbed species, adatoms, etc.

Kinetics of Water Exchange. The $W(r)$ for the barium-oxygen on water pair for the aqueous cation and surface bariums on the {001} barite surface are shown in Figure 2. The maximum in the $W(r)$ defines the transition state distance, which is 376 pm for the aqueous ion and 368 pm for ions on the surface (Table 1). Equation 2 is used to calculate the k_{TST} for these distances, with $k_{TST} = 2.4 \times 10^{10}$ s^{-1} for the aqueous barium ion and 9.9×10^{10} s^{-1} for the ion on the surface, some ~4 times larger.

When the transmission coefficient is calculated, there is some difficulty in defining the transition state. If only the ion−water distance is used to define the reaction coordinate, this gives an unphysical result: the constrained water molecule rotates such that its protons point at the oxygens on other water molecules in the first shell of the barium ion. We attribute the cause of this phenomenon to the large size of the barium ion. If this definition of the reaction coordinate is used, the time-dependent transmission coefficient calculation does not converge onto a plateau value because the exchanging water molecule moves away from the barium ion within a few time steps regardless of its initial velocity. Clearly, using only an ion−water distance is not a sufficiently good definition of the reaction coordinate. A solvent organization parameter and/or a more complex reaction coordinate definition are necessary.[42]

As an intermediate measure, the average water orientation at $r^{\ddagger} \pm 0.1$ pm was determined from the unconstrained simulations used to determine the $W(r)$. A harmonic Ba−O−H angle constraint at the average orientation was then added to the exchanging water molecule and the barium ion in the simulations that generated the initial configurations for the transmission coefficient estimate. For the aqueous barium ion this orientation was 108.8° and 84.5° for the barite surface. The results from which the transmission coefficients are derived are shown in Figure 3. The plateau value of $\kappa(t)$ is 0.20 for the aqueous ion and 0.17 for the surface (Table 1). The overall rate constant for water exchange for the aqueous barium ion is calculated to be $k = 4.8 \times 10^9$ s^{-1}, consistent with experimental estimates of 10^9−10^{10} s^{-1}. A correlation function fit[43] yields an apparent rate constant of 1.8×10^{10} s^{-1}, larger than the rate constant calculated via reactive flux. Previous calculations on aqueous barium ion using the same method yielded a rate constant of 7.6×10^9 s^{-1}.[26] Although in the reactive flux method one is forced to constrain the reaction coordinate, we believe it likely that it is the more accurate of the two methods, since it is derived from the average over an entire simulation data set. In a correlation function fit, a limited number of exchanges is used each time a fit is used (where the maximum is equal to the coordination number). Additionally, in the correlation function there is a somewhat arbitrary distinction as to what constitutes an exchange, i.e., the water must exchange for greater than 2 ps to be considered.[43]

The overall rate constant for water exchange of the barium ions on the barite surface is $k = 1.7 \times 10^{10}$ s^{-1}, 3.5 times larger than that of the aqueous ion. The larger rate constant on surfaces relative to the aqueous ion is consistent with the rates of aluminum containing minerals vs the aqueous aluminum

TABLE 1: Water Structure and Exchange Results.

	n_{coord}	$r_{first\ shell}$ (pm)	$r^{\ddagger}$(pm)	k_{TST} (s^{-1})	∠Ba−O−H for $k(t)$ (deg)	$k(t)$	k (s^{-1})	τ (ps)
Ba_{aq}	8.3	280	376	2.4×10^{10}	108.9	0.20	4.8×10^{9}	208
			376	2.4×10^{10}	125.3	0.20	4.8×10^{9}	208
			368	2.7×10^{10}	125.3	0.21	5.7×10^{9}	175
Ba_{barite}	0.9	282	368	9.9×10^{10}	84.5	0.17	1.7×10^{10}	59
			368	9.9×10^{10}	125.3	0.12	1.2×10^{10}	83

cation.[14] However, on a more similar material, calcite, calculated water residence times were longer on mineral surfaces relative to the aqueous calcium ion, yet retained similar bond lengths,[15] as is found here. The corresponding water exchange rate constants were approximately an order of magnitude smaller for the surfaces relative to the aqueous ions, a result not observed in the present study. This suggests that the calcite−water interface hinders water exchange whereas the barite−water interface does not.

Finally, it is desirable to be able to attribute some physical significance to the relative estimates of $\kappa(t)$ and k_{TST} for the aqueous ion and the surface. Yet, as mentioned previously, the estimated rate constants are sensitive to the choice of transition state and only the overall rate may be meaningful.[20,21] In this case, errors could arise from either an incorrect $r^{\ddagger}$ distance or a deviation in the exchanging water's orientation, in this case the Ba−O−H angle. A sensitivity analysis was performed to better understand how these parameters affect the rate constant estimate. First, the orientation of the exchanging water molecule was changed from the average orientation to 125.3° (the largest Ba−O−H angle possible while having both protons equidistant from the barium). The estimate of $\kappa(t)$ remains the same for the aqueous ion (Table 1). Second, the $r^{\ddagger}$ distance for the aqueous barium ion was changed to that of the surface exchange, 368 pm. In this case, $k_{TST} = 2.7 \times 10^{10}$ s^{-1}, which is slightly larger than the original estimate (2.4×10^{10} s^{-1}). The $\kappa(t)$ estimate is slightly higher at 0.21, but well within the uncertainty. The overall rate constant is 5.7×10^{9} s^{-1}, an increase of ~20% over the original rate estimate. For the barite surface, using a 125.3° Ba−O−H angle results in a lower $\kappa(t)$ at 0.12, which is a small change but significantly different from the original estimate of 0.17. This lowers the overall rate constant estimate by ~30% to 1.2×10^{10} s^{-1}. In one respect, variation of 20−30% in the rate constant estimates is minor relative to the 20 orders of magnitude variation in water exchange rates for aqueous cations,[8] but this result emphasizes that the choice of the reaction coordinate and transition state significantly affects the predicted rate.

Conclusions

The structure and kinetics of water exchange on aqueous barium ion and barium ions on the {001} surface of barite were estimated by using molecular dynamics. The structure of the aqueous barium ion matches experimental estimates, with an average coordination number of 8.3 and a first shell water distance of 280 pm. However, the {001} barite−water interface oxygen structure is somewhat inconsistent to estimates made by X-ray reflectivity. The rate constant for water exchange on an aqueous barium ion is $k = 4.8 \times 10^{9}$ s^{-1}, consistent with the experimental estimate. k_{TST} is 2.4×10^{10} s^{-1} and $\kappa(t)$ is 0.20. For barium ions within the barite surface, the overall rate constant is 2−3.5 times faster, with best estimates of $k = 1.7 \times 10^{10}$ s^{-1}. k_{TST} is 9.9×10^{10} s^{-1} and $\kappa(t)$ is 0.17.

Acknowledgment. The authors are grateful to Paul Fenter of Argonne National Laboratory for his help interpreting the XRR data and fit and William Casey for his fruitful discussions regarding water exchange. Support for this work came from the U.S. DOE Grants DE-FG02-07ER15901 (A.G.S.) and DE-FG02-04ER15498 (J.R.R.).

References and Notes

(1) Samson, S. D.; Stillings, L. L.; Eggleston, C. M. *Geochim. Cosmochim. Acta* **2000**, *64*, 3471−3484.

(2) Casey, W. H.; Ludwig, C. *Rev. Mineral.* **1995**, *31*, 87−117.

(3) Dove, P. M.; Czank, C. A. *Geochim. Cosmochim. Acta* **1995**, *59*, 1907−1915.

(4) Rosenqvist, J.; Casey, W. H. *Geochim. Cosmochim. Acta* **2004**, *68*, 3547−3555.

(5) Fenter, P.; McBride, M. T.; Srajer, G.; Sturchio, N. C.; Bosbach, D. *J. Phys. Chem. B* **2001**, *105*, 8112−8119.

(6) Fenter, P.; Sturchio, N. C. *Prog. Surf. Sci.* **2004**, *77*, 171−258.

(7) Hofer, T. S.; Rode, B. M.; Randolf, B. R. *Chem. Phys.* **2005**, *312*, 81−88.

(8) Richens, D. T. *The Chemistry of Aqua Ions*; John Wiley & Sons: New York, 1997.

(9) Margerum, D. W.; Cayley, G. R.; Weatherburn, D. C.; Pagenkopf, G. K. In *Coordination Chemistry*; Martell, A. E., Ed.; ACS Monograph No. 174; American Chemical Society: Washington, DC, 1978.

(10) Spångberg, D.; Rey, R.; Hynes, J. T.; Hermansson, K. *J. Phys. Chem. B* **2002**, *107*, 4470−4477.

(11) Rustad, J. R.; Stack, A. G. *J. Am. Chem. Soc.* **2006**, *128*, 14778−14779.

(12) Masia, M.; Rey, R. *J. Phys. Chem. B* **2003**, *107*, 2651−2659.

(13) Rey, R.; Hynes, J. T. *J. Phys. Chem.* **1996**, *100*, 5611−5615.

(14) Wang, J.; Rustad, J. R.; Casey, W. H. *Inorg. Chem.* **2007**, *46*, 29620−2964.

(15) Kerisit, S.; Parker, S. C. *J. Am. Chem. Soc.* **2004**, *126*, 10152−10161.

(16) Rushdi, A. I.; McManus, J.; Collier, R. W. *Marine Chem.* **2000**, *69*, 19−31.

(17) Paytan, A.; Kastner, M.; Chavez, F. P. *Science* **1996**, *274*, 1355−1357.

(18) Bertram, M. A.; Cowen, J. P. *Aquat. Geochem.* **1998**, *4*, 455−468.

(19) Sternberg, E.; Tang, D.; Ho, T.-Y.; Jeandel, C.; Morel, F. M. M. *Geochim. Cosmochim. Acta* **2005**, *69*, 2745−2752.

(20) Chandler, D. *J. Chem. Phys.* **1978**, *68*, 2959−2970.

(21) den Otter, W. K.; Briels, W. J. *J. Am. Chem. Soc.* **1998**, *120*, 13167−13175.

(22) Eyring, H. *J. Chem. Phys.* **1935**, *3*, 107−115.

(23) Jang Y. H.; Chang X. Y.; Blanco M.; Hwang S.; Tang Y.; Shuler P.; Goddard, W. A., III *J. Phys. Chem. B* **2002**, *106*, 9951−9966.

(24) Mayo, S. L.; Olafson, B. D.; Goddard, W. A., III *J. Phys. Chem.* **1990**, *94*, 8897−8909.

(25) Levitt, M.; Hirshberg, M.; Sharon, R.; Laidig, K. E.; Daggett, V. *J. Phys. Chem. B* **1997**, *101*, 5051−5061.

(26) Piana S.; Jones, F.; Gale, J. D. *J. Am. Chem. Soc.* **2006**, *128*, 13568−13574.

(27) Allan N. L.; Rohl A. L.; Gay D. H.; Catlow R. A.; Davey R. J.; Mackrodt W. C. *Faraday Discuss.* **1993**, *95*, 273−280.

(28) Plimpton, S. J. *J. Comput. Phys.* **1995**, *117*, 1−19. http://lammps.sandia.gov/

(29) Swope, W. C.; Anderson, H. C.; Berens, P. H.; Wilson, K. R. *J. Chem. Phys.* **1982**, *76*, 637−649.

(30) Nosé, S. *Mol. Phys.* **1984**, *52*, 255.

(31) Nosé, S. *J. Chem. Phys.* **1985**, *81*, 511.

(32) Hoover, W. G. *Phys. Rev. A* **1985**, *31*, 1695.

(33) Ryckaert, J. P. *Mol. Phys.* **1985**, *55*, 549−556.

(34) Eisenberg, D.; Kauzmann, W. *The Structure and Properties of Water*; Oxford University Press: Oxford, UK, 1969.
(35) Soper, A. K.; Phillips, M. G. *Chem. Phys.* **1986**, *107*, 47−60.
(36) Berendsen, H. J. C.; Grigera, J. R.; Straatsma, T. P. *J. Phys. Chem.* **1987**, *91*, 6269−6271.
(37) Mark, P; Nilsson, L. *J. Phys. Chem. A* **2001**, *105*, 9954−9960.
(38) Persson, I.; Sandström, M.; Yokoyama, H.; Chaudhry, M. *Z. Naturforsch.* **1995**, *50a*, 21−37.
(39) Cannon, W. R.; Pettitt, B. M.; McCammon, J. A. *J. Phys. Chem.* **1994**, *98*, 6225−6230.
(40) Ohtaki H.; Radnai, T. *Chem. Rev.* **1993**, *93*, 1157−1204.
(41) Marcus, Y. *Ion Solvation*; Wiley: New York, 1985**.**
(42) Schenter, G. K.; Garret, B. C.; Truhlar, D. G. *J. Chem. Phys.* **2003**, *119*, 5828−5833.
(43) Impey, R. W.; Madden, P. A.; McDonal, I. R. *J. Phys. Chem.* **1983**, *87*, 5071−5083.

Molecular Dynamics Simulations of Solvation and Kink Site Formation at the {001} Barite−Water Interface†

Andrew G. Stack*

School of Earth and Atmospheric Sciences, Georgia Institute of Technology, 311 Ferst Drive, Atlanta, Georgia 30332-0340

Received: July 16, 2008; Revised Manuscript Received: September 29, 2008

Solvation and kink site formation on step edges are known to be controlling parameters in crystal growth and dissolution. However, links from classical crystal growth models to specific reactions at the mineral−water interface have remained elusive. Molecular dynamics is used here to examine the water structure on barium surface sites and kink site formation enthalpies for material adsorbed to and removed from the step parallel to the [120] direction on the {001} barite-water interface. The bariums at the interface are shown to be coordinatively unsaturated with respect to water, and it is suggested that this is due to a steric hindrance from the nature of the interface. Kink site detachment energies that include hydration energies are endothermic for barium and exothermic for sulfate. The implications and problems of using these parameters in a crystal growth model are discussed.

Introduction

The molecular-level chemical reactions that control the growth and dissolution of crystalline materials affect a number of large-scale environmental processes. These processes include reactions that affect ground and surface water quality, rock and soil weathering, contaminant transport and remediation, and biomineralization. One challenge facing geochemists is to develop physically realistic models that quantitatively predict the kinetics of mineral growth and dissolution under a variety of conditions. The classical theory used to model the growth of a crystal was developed in large part by Burton, Cabrera, and Frank.[1] In this theory, the net rate of growth or dissolution is determined by the difference in the rates of attachment and detachment of idealized "growth units," or nondivisible building blocks of crystals. For example, aqueous ions that precipitate can be thought of as the growth units for a mineral. The rate of attachment is controlled by the concentration of growth units in solution and dehydration reactions, whereas the rate of detachment is controlled by the bonding environment for a surface site and hydration reactions. At saturations near equilibrium, growth and dissolution occur by advance and retreat of monomolecular steps on the crystal surface that originate from pre-existing structural defects in the crystal.[2,3] The movement of these steps in turn is controlled by defects within the step structure known as kinks. Growth units can attach to an otherwise uniform step, nucleating a positive kink, or detach from an otherwise uniform step, forming a negative kink (Figure 1). Once nucleated, kink sites can propagate along the length of the step.

The classical crystal growth model provides a useful framework to understand growth and dissolution reactions. However, it is difficult to relate the model to specific reactions occurring on mineral surfaces because it was designed for simple materials, that is, single-component crystals with a simple cubic lattice that grow from a vapor. Typical soil and near-surface minerals include at least two components and often contain multiple orientations or bonding environments per component. To complicate matters further, dissociative adsorption of water as either a reactant or an intermediate[4] and background electrolyte concentration[5,6] are known to affect growth rate. Specific mechanisms for growth and dissolution reactions remain largely speculative due to this complexity.

Atomistic computational simulations are attractive to use to model crystal growth because a given reaction thought to be important can be defined precisely. The accurate simulation of surface reactions requires a large number of atoms, however, and hitherto, most often, calculations have been made in the gas phase without consideration of the solvent. This leads to an overestimation of the energies of given reactions because the solvent reduces the interfacial energy and the large exothermic hydration energy of ions is neglected as well. A correction for the hydration energy can be made, but it is difficult to estimate accurately because it is not known what fraction of the hydration energy is retained by a given species while attached to the surface.[5]

The aims in the present work are, first, to calculate the coordination number of various surface sites in the first hydration shell and the fraction of the hydration shell that is retained for various surface species thought to exist at the {001} barite−water interface. Second, we calculate kink site formation energies for 10 different kink site nucleation reactions on the steps parallel to the [120] direction on the {001} barite−water interface. The [120] step was chosen because it is one of two dominant step orientations found on the {001} surface and is the only orientation that follows a periodically bonded chain.[5] The estimated kink site formation energies are compared to experimental measurements of step velocities on barite to better understand kink site nucleation and, hence, step velocity during barite growth and dissolution.

Barite was chosen because it often forms in ocean water and sediments, and its presence is used as an indicator of primary productivity.[7] It is also used as a biomineral by some benthic organisms, foraminifera, and algae.[8] Previous computational work on barite includes analyses of the equilibrium morphology

† Part of the special section "Physical Chemistry of Environmental Interfaces".

* E-mail: andrew.stack@eas.gatech.edu.

10.1021/jp8062993 CCC: $40.75
Published on Web 11/06/2008

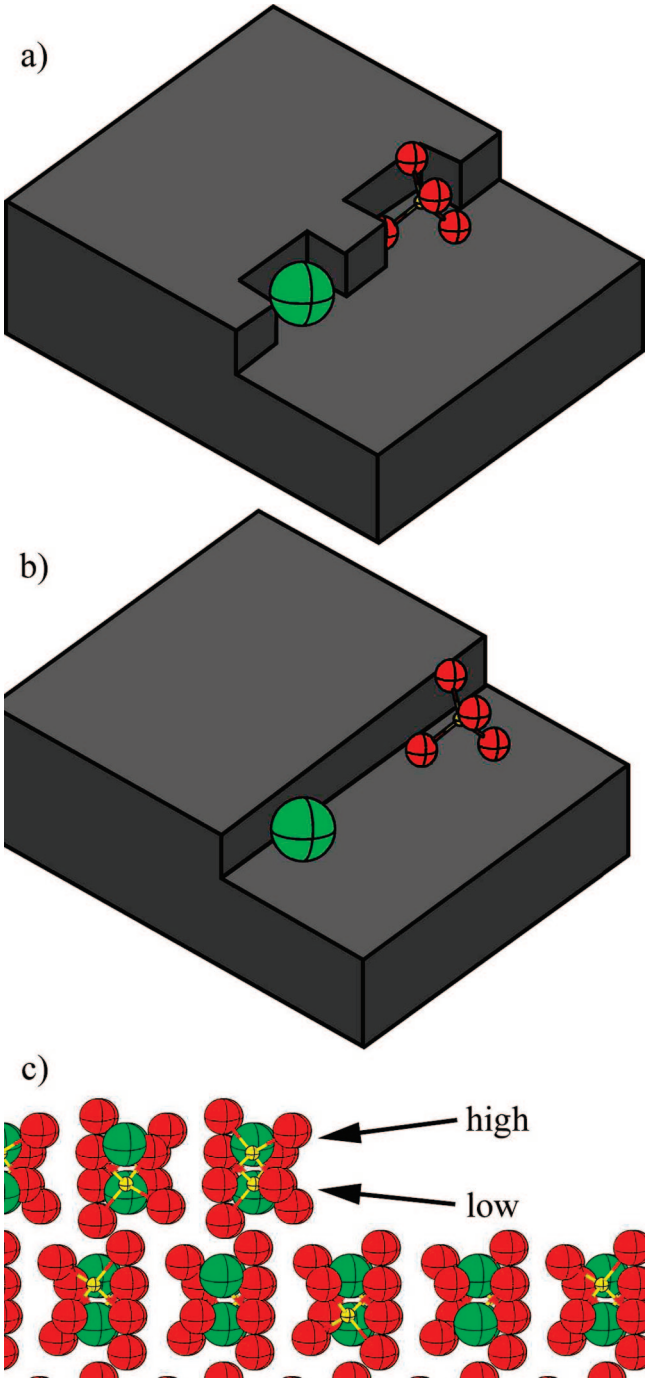

Figure 1. Diagram showing the structure of modeled kink site formation energies for steps parallel to the [120] direction on the {001} barite surface. (a) Barium or sulfate ions can detach from what started as a smooth step, leaving behind a negative kink. Prior to detachment, ions in these positions are referred to as step-edge sites. (b) Similarly, barium and sulfate ions that are adsorbed to the edge of a smooth step form a positive kink. (c) Cross-sectional view of the same step. Both barium and sulfate ions are found in two separate structures, high and low, while embedded within a surface or adsorbed to a surface.

in vacuo[9] and with explicit consideration of the solvent,[10] nucleation energy for island growth[11] and growth inhibition[5] *in vacuo* with a correction for solvation, barium adsorption to planar barite−water interfaces,[12] and water exchange rates of aqueous barium ion and the barite−water interface.[13]

Computational Methods

Here, we build upon our existing implementation[13] of a molecular dynamics force field developed by Jang et al.[10] with the F3C water model[14] adapted to the LAMMPS software package.[15] The short-range forces included columbic interactions and Van der Waals forces as well as bonded interactions. Van der Waals forces were modeled using Buckingham potentials between pairs of the constituent atoms of barite (Ba, S, $O_{sulfate}$) and the interaction of these atoms with atoms in water (O_{water}, H). Pair potentials between the constituent atoms in water are modeled using a Lennard−Jones potential. The S−$O_{sulfate}$ and O_{water}−H bonds are treated with a harmonic potential that restrains the bond length. Orientation is enforced using a harmonic cosine potential on the $O_{sulfate}$−S−$O_{sulfate}$ angles and a harmonic restraint on H−O_{water}−H. Bond-bond terms and angle-angle potentials between $O_{sulfate}$ and S atoms are included to more accurately model the vibrational frequencies of sulfate. See the Supporting Information, Table S1, for the functional form and parameters used in the model.

The calculation of short-range forces was cut off at distances greater than 10 Å, and therefore, the scaling parameter on the F3C water model was set to 1.0.[14] All Lennard−Jones terms were shifted to zero at their cutoff. The Ewald sum was used to calculate the columbic potential energy at distances greater than the cutoff with a tolerance of 1×10^{-4}. When a charged cell is used, LAMMPS automatically performs a correction to the electrostatic energy.[16] The time-step used was 1 fs, and all simulations were run for at least 1×10^7 timesteps (10 ns), with the first 1 ns discounted as equilibration time. Energy differences were averaged over the last 9 ns of these simulations, where the potential energy was sampled every 10 time steps. Hydration energies were calculated as the difference in average potential energy of a periodic 20 × 20 × 20 Å simulation cell of 267 water molecules with a separate ion and the same-sized cell of the same number of water molecules including an ion.

A periodic simulation cell was used to calculate kink site formation energies with a size of 34.4475 × 28.1422 × 57.2552 Å, half of which was water (in the z direction). It contained 280 $BaSO_4$ formula units and 1041 water molecules (Figure 2). To ensure accuracy of kink site formation energies, the step would have been ideally at least as long as the distance between kink sites. Presumably, the kink density on barite is low enough that this would be computationally prohibitive, but here, the cell is four formula units long (Figure 2b). While removing or adding ions to the step edge, two ions were always removed or added to minimize surface dipole moments, one from the step on top of the barite slab and one from the step on the bottom side. Detachment energies for ions were calculated by taking the difference in average potential energies between the step containing the undissolved species, the step with the species dissolved, and the hydration energy of the dissolved species. For consistency, these were always calculated as products minus reactants and written as detachment reactions. So, for example, a negative kink site formation reaction for barium ion is $E_{\text{kink detachment}} = \{E_{\text{step missing 2 Ba ions}} + (2 \times E_{\text{hydration Ba ion}}) - E_{\text{full step}}\}/2$. The kink site detachment energy for a positive kink is $E_{\text{kink detachment}} = \{E_{\text{full step}} + (2 \times E_{\text{hydration Ba}}) - E_{\text{step with 2 Ba ions added}}\}/2$. Detachment energies for sulfate follow similar expressions. Coordination numbers were calculated by averaging the number of water molecules sampled every 100 time steps for at least 1 ns of simulation using an equilibrated structure. The average Ba−O_{water} distance for the transition state on the water exchange reaction for bariums on the barite surface, 368 pm, was used as the cutoff for first-shell water.[13] Ba−$O_{sulfate}$ bond distances were calculated by averaging over specific oxygens on sulfates selected by hand due to substantial overlap in the radial distribution functions.

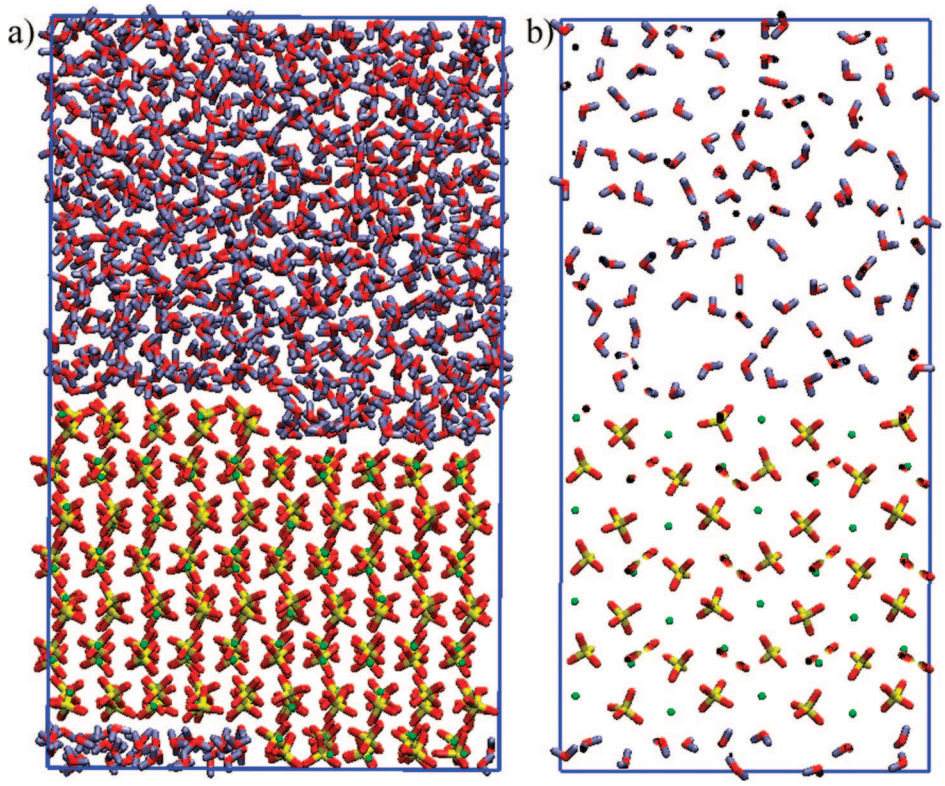

Figure 2. Supercell used in calculations. (a) View along the [120] direction, parallel to the step. (b) Cross-sectional slice through the center of the cell cut perpendicular to the [120] direction, showing the step-edge is four formula units long.

TABLE 1: Thermodynamic and Structural Parameters for the Barite-Water System

		original	alternate	reference estimate(s) and source(s)	
$\Delta H_{lattice}$ barite (kJ/mol)		−2480	−2480	−2478	est. from calorimetric data[10]
$\Delta H_{surface}\{001\}$ barite (mJ/m^2)	vacuum	487	487	400−616	other MD[9,10]
	solution	284	20	24.6	ζ-potential and contact angle[17]
$\Delta H_{hydration}$ (kJ/mol)	H_2O	−42	−42	−41.5	calorimetry[18]
	$Ba_{(aq)}$	−1135	−1301	−1305	calorimetry[19,20]
	$SO_{4(aq)}$	−1045	−1096	−1108	calorimetry[19]
coordination number	$Ba_{(aq)}$	8.3	8.8	8.1	LAXS, EXAFS[19,20]
	$SO_{4(aq)}$	15	16	7−13	computational est.[21−23]
bond length (pm)	$Ba_{(aq)}-O_{water}$	280	276	282	LAXS, EXAFS[20]
	$SO_{4(aq)}-O_{water}$	385	381	361−393	various[21−23]

Results and Discussion

Molecular Dynamics Force Fields. Our previous implementation of this force field underestimated the hydration energy of the aqueous ions (labeled "original" in Table 1).[13] To correct this, the $Ba-O_{water}$ and $O_{sulfate}-O_{water}$ pair potentials were modified to fit experimental hydration energies while attempting to minimize the change to bond length between the ion and the first shell water ($r_{first\ shell}$) and coordination number (parameters for both models are shown in the Supporting Information). The revised model substantially improves the estimated hydration and surface energies, but the structures on the aqueous ions are modeled less well (labeled "alternate" in Table 1). The agreement between the calculated surface free energy and an experimental measurement of a hydrated barite surface free energy from ζ-potential and contact angle measurements[17] provides an independent confirmation of the alternate model as it was not a fit parameter. The lattice energy of the barite ($\Delta H_{lattice}$), the vacuum surface energy ($\Delta H_{surface}$), and the heat of vaporization of water ($\Delta H_{hydration}$) do not change between the original and alternate models because the parameters that control these were not changed. Although there is no experimental measurement of coordination number of aqueous sulfate ion and computational estimates are poorly constrained, it is probable that the coordination number on the aqueous sulfate is overestimated in both models. Thus, the coordination of surface sulfates is not examined closely here, only barium. Because of the differences in accuracy in these two models, in the subsequent results and discussion, the original model was used when a coordination number or a bond length is reported. When an energy is reported, the alternate model has been used. Encouragingly, if the error in the aqueous ion hydration energy for the original model is used as a correction factor for kink site formation energies calculated using the original model, the two models give energies of similar magnitude (data not shown)

Water Coordination on Surface Bariums. To compare coordination environments, the coordination number for oxygens on the first shell water was plotted as a function of the coordination number for oxygens on the sulfate to which each

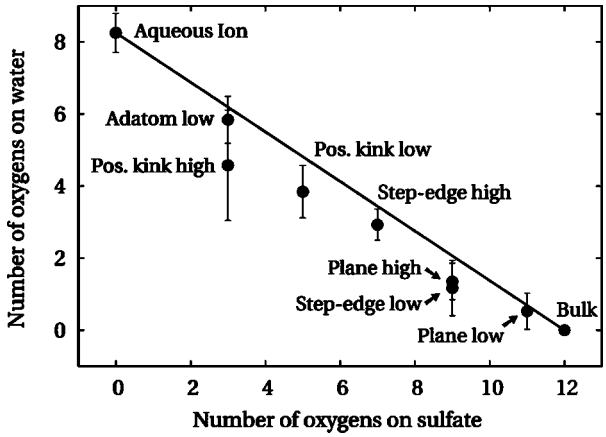

Figure 3. Coordination environments for barium surface sites. The high or low positions refer to the sites shown in Figure 1c. Adatom refers to an ion adsorbed to the {001} surface, Pos. kink indicates a positive kink (Figure 1b), step-edge refers to ions embedded in the step-edge shown (Figure 1a), and plane refers to ions embedded within the {001} surface. In an ideal system, for every surface structure that contains a reduced number of bonds to the mineral surface (oxygens on sulfate), these would be replaced by a proportional number of bonds to a water molecule (oxygens on water). This ideal case is represented by the straight line; points that plot below this line are under-coordinated by water.

site is bonded (Figure 3). The two end members in this system are barium in the bulk, coordinated to 12 oxygens on sulfate and 0 oxygens on water, and aqueous barium ion, which is coordinated to 8.3 oxygens on water and 0 oxygens on sulfate. To understand the relationship for structures that lie in between these two end members, consider the bonding environment of barium in this system: the hydration of large, second-group aqueous cations such as barium is best explained by the ratio of size to charge[19] and the packing density of liquid water molecules. Furthermore, the bonding between barium and sulfate in barite is dominantly ionic,[24] as evidenced by its high melting point, 1580 °C. The bonding orbitals for barium are the spherically symmetric 6s orbitals, whereas the bonding 2p orbitals on oxygen are anisotropic, but the anisotropy of the interaction of these orbitals with barium or water has not been found necessary to consider explicitly in MD simulations of this system, nor vacant higher-level orbitals.[5,9−12,21] As a result, MD models describe the interaction between barium and oxygens (on both sulfate and water) using the same functional form of isotropic Coulombic attraction and Van der Waals forces.[10,12,13] A consequence of this is that the ratio of size to charge and the efficiency of packing of bariums and sulfates also determine the barium coordination to oxygen in barite in this model, as with the aqueous ion. For any given surface site, the idealized behavior would be one in which the transition from the coordination environment of bulk barite to that of the aqueous ion would be smooth. In this idealized behavior, each surface structure that is coordinated to a reduced number of oxygens on sulfate relative to the bulk ought to be replaced by a proportional number of oxygens on water, on average. This proportionality is represented by the straight line connecting the aqueous and bulk barium ions. The average water coordination of surface sites ranges from slight to significant deviation from this line, indicating that all barium surface structures are coordinatively unsaturated with respect to water relative to what they ought to be if they were ideally compensated for the missing sulfates. The most extreme "under-coordination" is found in the barium adsorbed to a step-edge (forming a positive kink) in the high position with 1.6 fewer water molecules than the ideal case. This site also has a relatively large standard deviation in the coordination number, 1.5, that indicates water molecules often exchange on the site. In the remainder of the sites, the under-coordination ranges from 0.2 water molecules for bariums embedded in the low position in the {001} surface (plane low) to 1.0 water molecules for bariums adsorbed to the step edge in the low position (Pos. kink low) with an average of 0.6.

TABLE 2: Calculated Detachment Energies[a]

site	negative kink (kJ/mol)	positive kink (kJ/mol)
Ba high	+195	+144
Ba low	+188	+149
SO_4 high	−38	−83
SO_4 low	−11	−95
$BaSO_4$ high	+122	+114

[a] Explanation of the various types of sites are shown in Figure 1.

It is conceivable that the under-coordination by water is driven by relaxation of the surface sulfates or variability in the bonding environment between sites. In bulk barite, $Ba-O_{sulfate}$ bond lengths can vary from 277 to 331 pm, with an average of 295 pm.[25] This model gives a similar range of $Ba-O_{sulfate}$ bond lengths, with an average of 296 pm. If the bonding environment to sulfate were causing the under-coordination changes to water, one would expect the average $Ba-O_{sulfate}$ bond length to the sulfates to be shorter for sites more under-coordinated by water. For each surface site, the average bond length decreases weakly with decreasing coordination numbers for $O_{sulfate}$; for example, $Ba-O_{sulfate}$ 295 pm for bariums in the step edge in the low position to 290 pm for those in the high position to 288 pm for positive kinks in the low position to 286 pm for those in the high position. Since there is no correlation between $Ba-O_{sulfate}$ bond length and the under-coordination, surface relaxation of sulfates and the barium-to-sulfate bonding environment does not seem to be causing the observed under-coordination.

One possibility is that access by water to the sites may be sterically hindered due to the geometry of each site and the presence of the interface. A steric effect explains why the positive kink in the high position and the adatom in the low position have the same coordination for oxygens on sulfate but differing coordination for oxygens on water (Figure 3). The bond lengths to sulfate for these two sites are similar: the average $Ba-O_{sulfate}$ bond length is 285 pm for the adatom site and 286 pm for the positive kink site in the high position. It is then likely that a steric hindrance is causing the observed under-coordination for this and other sites that is predicted in this model. Thus, the total coordination to water for a given site appears to to be driven by a combination of the coordination to sulfate and the physical access to the site by water.

Kink Site Detachment Energies. There are substantial differences in calculated detachment energy between various types of kink sites on steps aligned parallel to the [120] direction, as shown in Table 2. First, detachment of ions from positive kinks is always more favorable than detachment to form negative kinks. The step-edge sites that form negative kinks retain a larger number of bonds to the surface than the positive kinks (Figure 3), which is evidently more favorable than having a larger number of bonds to the solvent. The trend is consistent with a surface energy perspective; the undisrupted full step is a relatively low-energy structure relative to the kink sites. To form a negative kink from a full step therefore requires correspondingly more energy than to form a full step after removing the higher energy positive kink site. For ions in the low and high positions, there is a smaller difference in detachment energy

within a single type of kink, but the relative favorability of detachment reverses for positive and negative kinks. For example, bariums in low sites are more favorable to detach to form negative kinks than bariums in high sites, whereas they are less favorable to detach from positive kinks than high sites. These relative favorabilities of detachment are consistent with the degree of under-coordination of the same sites in Figure 3. Bariums that form the positive kinks in the high position are more under-coordinated than bariums that form positive kinks in the low position and have a correspondingly lower detachment energy. Similarly, the ions on the step edge that detach to form negative kinks that are in the low position are more under-coordinated than those in the high position and have a more favorable detachment energy. The water coordination environment for surface species thus plays a role in determining the relative detachment energies of different sites.

We assume that the attachment of positive kinks is an important reaction for growth and detachment of negative kinks during dissolution; to determine the attachment energy for positive kinks, the sign of the detachment energy is reversed. If the attachment energy for positive kinks and the detachment energy for negative kinks is compared, the sum is always positive, meaning that detachment energy of negative kinks is always more unfavorable than attachment of positive kinks is favorable.

The most striking feature of the data in Table 2 is that detachment of barium ions is substantially less favorable than detachment of sulfate ions. The relative favorabilities of detachment of bariums versus sulfates is consistent with free energy profiles made for calcium and carbonate detachment on the similar material calcite, where it has been shown that the cation requires more energy to detach than the anion.[26] Calcite and barite are similar in that they are composed of group 2 cations and oxyanions and are sparingly soluble salts. One difference between the previous work on calcite and the present work is that, here, sulfate ion detachment is exothermic, whereas on calcite, the carbonate detachment energy was found to be smaller than that of calcium but still endothermic.[26] Exothermic sulfate detachment is internally consistent with qualitative observations of these simulations wherein temporary disordering of sulfates on the {001} surface and even rotations in place occurred occasionally.

It requires less energy to remove a formula unit ($BaSO_4$ high in Table 2) from the surface and dissociate the constituent ions in solution than detach the individual ions themselves. It costs +122 kJ/mol of energy to form a negative $BaSO_4$ kink, which is 35 kJ/mol more favorable than the sum of the Ba and SO_4 detachment energies of the same type of site. The gain is likely due to the creation of a lower-energy uncharged surface and, in the case of a negative kink, greater access of water to the site. Detachment of the $BaSO_4$ positive kink site is less favorable than detachment of the constituent ions as their own negative kink site by 53 kJ/mol. This is probably due to the stabilization of the positive kink by the addition of more material[11] and relief from the relatively large degree of under-coordination of the barium in the positive kink site by water by a larger coordination to the sulfate (Figure 3).

The classical model for crystal growth calls for kink site formation to be driven by thermodynamics,[1] and the step is assumed to be in local equilibrium with respect to kink site density. The density of kinks on a step, ρ (number of kinks per unit cell), at a given temperature, T, follows a Boltzmann distribution that depends on the kink site formation energy, ε,

$$\rho = 2e^{-\varepsilon/kT} \quad (1)$$

where k is the Boltzmann constant.[1,27] For nonequilibrium conditions, the kink density will include a saturation term that reflects the flux of material to the surface from solution.[27] If a classical model for [120] step movement is assembled using the present simulations, both a forward-reaction for growth (e.g., attachment to positive kinks) and a back-reaction (detachment from those same kinks) would need to be considered. Starting with the back-reaction, a detachment energy of +144 or +149 kJ/mol for barium ions to form positive kinks means that detachment essentially does not occur with any great frequency at room temperature. This implies that the back-reaction during growth is negligible. For the forward reaction, the attachment energy would be −142 or −149 kJ/mol; the negative sign indicates that attachment would be limited by the rate of diffusion of barium ions to the step. For sulfate, the reverse is true. Since the detachment during the back-reaction is exothermic, it would occur as fast as sulfate can diffuse away from the step, and attachment during the forward reaction would be required to be +83 or +95 kJ/mol. Using equation 1, the kink spacing for the average forward reaction is too high to be realistic, 2×10^{15} unit cells/kink, which corresponds to one kink every 10^6 meters. Finally, the relative favorabilities of the forward reactions calculated here are not consistent with recent experimental data that suggests that barium attachment is the limiting step velocity because an excess in the aqueous barium concentration leads to a faster step velocity than a 1:1 ratio of barium to sulfate or an excess of sulfate.[28] The discrepancy between the present model and these results suggests the kinetics of the reaction-determining step velocity do not follow the potential energy differences as calculated here. Recent work has shown that the free energy surface for attachment and detachment of barium ions to the {001} surface of barite contains more than one minimum and maximum,[12] and similar observations have been made for calcite.[29] From this we surmise that the mechanism of attachment or detachment to a kink site is similarly complex in that attachment and detachment proceed through some intermediate structures whose rate of formation limits the step velocity. If this were true, the magnitude of the attachment and detachment energies of barium versus sulfate calculated in Table 1 may be proportional to the activation energies for the rate-determining step. In this case, barium attachment and detachment would have a larger activation energy and limit the step movement. Another possibility is provided by Kerisit and Parker,[29] who showed that the entropy of attachment and detachment could be significant. This would lead to a substantial change in the formation energies calculated from solely enthalpies here.

One important point is that in the classical model and most experimental measurements of step velocity, the rates of kink site formation for the anion and cation are assumed to be equal. Higgins et al.[30] used such an assumption to calculate a kink site formation energy during growth of +15 kJ/mol and an activation energy of +38 kJ/mol. In support of the experimental kinetic evidence,[28] the large difference in detachment energy for bariums and sulfates in Table 1 suggests that the kink site formation energies are not equal for barium and sulfate. However, we can estimate the apparent formation energy that would be measured by making an assumption of equal reactivity using the data in Table 1. Zhang and Nancollas[31] developed a model that accounted for variable attachment and detachment rates for both the cation and the anion. In this model, the kink site density, ρ, is

$$\rho = (r^{1/4} + r^{-1/4})e^{[-(\varepsilon_{Ba}+\varepsilon_{SO_4})/2kT]} \quad (2)$$

where ε_{Ba} and ε_{SO_4} are the kink site formation energy for barium and sulfate, respectively. The term r reflects the ratio of the rates of attachment and detachment barium to sulfate,

$$r = \frac{v_{SO_4} k_{Ba}[Ba^{2+}]}{v_{Ba} k_{SO_4}[SO_4^{2-}]} \quad (3)$$

where v_{Ba} and v_{SO_4} are the zeroth-order rate constants for detachment of barium and sulfate respectively, and k_{Ba} and k_{SO_4} are the first-order rate constants of attachment whose overall rate depends also on the aqueous concentrations of the ions $[Ba^{2+}]$ and $[SO_4^{2-}]$. Equation 2 simplifies to eq 1 if the ratio of the rates of attachment and detachment of the cation are the same as those of the anion (r in equation 3 becomes unity). As a first approximation, if r is assumed to be 1, the only difference between equations 1 and 2 would be that the apparent kink site formation energy in equation 1 would represent an average of the kink site formation energies for barium and sulfate. If the attachment energy for a positive kink is considered as the relevant reaction and the net attachment energy is the average of the high and low type sites, $\varepsilon_{Ba} = -147$ kJ/mol and $\varepsilon_{SO_4} = +89$ kJ/mol for sulfate kinks. The apparent formation energy in eq 1 is $\varepsilon = -29$ kJ/mol. This is of a similar magnitude as the experimental estimate (+15 kJ/mol),[30] but the negative sign on the formation energy is an apparently unphysical result. Yet, it is a direct consequence of the fact that barium attachment is an exothermic process in this model. The free energy of attachment of ions to calcite steps calculated previously is also exothermic.[26] Previous work on barium ion attachment to {001} surfaces resulted in an endothermic attachment, but if only a single adsorbed sulfate ion were adsorbed to the surface in the same locale prior to barium attachment, it was then exothermic.[12] Although kink site propagation reactions were not specifically accounted for here, it is unlikely that they will result in a reversal of the energetics of attachment. Taken together, it is unclear how computational models that consistently predict large exothermic attachment for cations to the step-edge can be reconciled with the standard physical interpretation that the kink site formation energy is due to attachment of ions to the step edge during growth directly from solution. More work to understand the mechanisms of attachment and detachment from a computational perspective is necessary because this could be the reason for the discrepancy. Another possibility is that the crystal growth model that is applied may need refinement. Chernov et al.[32] found that applying a model similar to that of Zhang and Nancollas[31] to AFM measurements of calcium oxalate step growth resulted in a ratio of detachment frequencies of calcium to oxalate that was negative, also an unphysical result.

Finally, a difference in kinetics of attachment and detachment (eq 3) might have an effect on the apparent kink site formation energy measured using eq 1. To simplify, we consider the case for the system at equilibrium with a 1:1 ratio of barium to sulfate, so the concentrations of the aqueous ions drop out of eq 3. Following the interpretation of back-reaction given above as detachment energies for positive kinks, we will assume that the rate of detachment of sulfate, v_{SO_4}, and the rates of attachment of barium, k_{Ba}, are limited by diffusion and are equal (diffusion coefficients for aqueous barium $= 8.47 \times 10^{-6}$ cm^2/s and aqueous sulfate $= 10.65 \times 10^{-6}$ cm^2/s are similar).[33] We will assume that the average detachment energy for aqueous barium for the high and low sites is a minimum estimate of the activation energy ($E_a = 146.5$ kJ/mol) that determines v_{Ba}, and the same for the attachment of sulfate ion ($E_a = 89$ kJ/mol) that determines k_{SO_4}. The rate constant for each is calculated by using an Arrhenius relationship, and we assume the prefactor, A, is the same for both barium and sulfate: $k = Ae^{(-E_a/RT)}$ (v is treated the same way). The resultant ratio of the rates is $r = e^{(-146.5/RT)}/e^{(-89/RT)} = 1.2 \times 10^{10}$ and the term $(r^{1/4} + r^{-1/4})$ is 331, just over 2 orders of magnitude larger than the case in which the rates of attachment and detachment are the same. Setting the different estimates of kink site density in eqs 1 and 2 equal to each other, one can estimate the error by assuming that the kinetics of attachment and detachment are the same,

$$\rho = (r^{1/4} + r^{-1/4})e^{(-\varepsilon_{int}/2RT)} = 2e^{(-\varepsilon_{app}/RT)} \quad (4)$$

where r is from eq (3), ε_{int} is the "intrinsic" kink formation energy, ε_{app} is the apparent kink site formation energy that would be observed by not accounting for differences in kinetics, and other symbols retain their usual meanings. Solving for $(r^{1/4} + r^{-1/4})$, ε_{int}, and ε_{app} gives

$$\varepsilon_{app} = \varepsilon_{int} - RT[\ln(r^{1/4} + r^{-1/4}) + RT \ln 2 \quad (5)$$

Thus, if $(r^{1/4} + r^{-1/4}) = 331$, ε_{int} would be underestimated by +12 kJ/mol. To illustrate, including the differences in the kinetics of attachment and detachment would mean the kink site formation energy of +15 kJ/mol measured by Higgins et al.[30] indicates an ε_{int} of +27 kJ/mol. This intrinsic kink formation energy is essentially the same magnitude as the average formation energy for the barium and sulfate kinks calculated above, yet the sign is again different. However, using these formation energies probably overestimates the activation energy. The activation energy for kink site formation/propagation was estimated as 38 kJ/mol for growth[30] and 25 kJ/mol for step movement during dissolution.[34] If an estimate is made for which the activation energy is 25% of the formation energies in Table 2 is used, the quantity $(r^{1/4} + r^{-1/4})$ is 4.5. This leads to a correction to ε_{app} of +4 kJ/mol, which is probably an order of magnitude similar to the error in estimating kink formation energies from step velocity measurements using the AFM.[35]

Conclusions

Solvation and kink site formation energy were examined for a variety of barite surface structures important for crystal growth and dissolution. It was found that barium surface sites are coordinatively unsaturated with respect to water, probably due to a steric hindrance that limits access of water to the sites located at the interface. Kink site detachment energies for barium kinks were found to be endothermic, whereas those of sulfate were exothermic; the relative favorabilities and magnitudes are not easily reconciled with crystal growth models and recent experimental evidence. It is suggested the discrepancy is because the mechanism for growth and dissolution and entropic contributions may affect the apparent kink site formation energy. Finally, it was shown that large differences in detachment and attachment rates between sulfate and barium as calculated here can lead to variation in the apparent kink site density if uniform site reactivity is assumed.

Acknowledgment. The author is grateful for support from the U.S. Department of Energy through grant DE-FG02-07ER15901 and Pacific Northwest National Laboratory, Environmental Molecular Sciences Laboratory, through user proposal 28091.

Supporting Information Available: Additional information as noted in text. This material is available free of charge via the Internet at http://pubs.acs.org.

References and Notes

(1) Burton, W. K.; Cabrera, N.; Frank, F. C. *Philos. Trans. R. Soc. London, Ser. A* **1951**, *243*, 299.

(2) De Yoreo, J. J.; Vekilov, P. G. *Rev. Mineral. Geochim.* **2003**, *54*, 57.

(3) Dove, P. M.; Han, N.; De Yoreo, J. J. *Proc. Nat. Acad. Sci. U.S.A.* **2005**, *43*, 15357.

(4) Shiraki, R.; Rock, P. A.; Casey, W. H. *Aquat. Geochim.* **2000**, *6*, 87.

(5) Becker, U.; Risthaus, P.; Bosbach, D.; Putnis, A. *Mol. Simul.* **2002**, *28*, 607.

(6) Dove, P. M.; Elston, S. F. *Geochim. Cosmochim. Acta* **1992**, *56*, 4147.

(7) Paytan, A.; Kastner, M.; Chavez, F. P. *Science* **1996**, *274*, 1355.

(8) Bertram, M. A.; Cowen, J. P. *Aquat. Geochem.* **1998**, *4*, 455–468.

(9) Allan, N. L.; Rohl, A. L.; Gay, D. H.; Catlow, R. A.; Davey, R. J.; Mackrodt, W. C. *Faraday Discuss.* **1993**, *95*, 273.

(10) Jang, Y. H.; Chang, X. Y.; Blanco, M.; Hwang, S.; Tang, Y.; Shuler, P.; Goddard, W. A., III *J. Phys. Chem. B* **2002**, *106*, 9951.

(11) Pina, C. M.; Becker, U.; Risthaus, P.; Bosbach, D.; Putnis, A. *Nature* **1998**, *395*, 483.

(12) Piana, S.; Jones, F.; Gale, J. D. *J. Am. Chem. Soc.* **2006**, *128*, 13568.

(13) Stack, A. G.; Rustad, J. R. *J. Phys. Chem. C* **2007**, *111*, 16387.

(14) Levitt, M.; Hirshberg, M.; Sharon, R.; Laidig, K. E.; Daggett, V. *J. Phys. Chem. B* **1997**, *101*, 5051.

(15) Plimpton, S. J. *J. Comp. Phys.* **1995**, *117*, 1; http://lammps.sandia.gov/ (accessed May 21, 2006). .

(16) Wasserman, E.; Rustad, J. R.; Felmy, A. R.; Hay, B. P.; Halley, J. W. *Surf. Sci.* **1997**, *385*, 217.

(17) Chibowski, E.; Hołysz, L. *J. Mater. Sci.* **1992**, *27*, 5221.

(18) Eisenberg, D.; Kauzmann, W. *The Structure and Properties of Water*; Oxford University Press: Oxford, 1969.

(19) Richens, D. T. *The Chemistry of Aqua Ions*; John Wiley & Sons: New York, 1997.

(20) Persson, I.; Sandström, M.; Yokoyama, H. *Z. Phys. D: At., Mol. Clusters* **1995**, *50a*, 21.

(21) Cannon, W. R.; Pettitt, B. M.; McCammon, J. A. *J. Phys. Chem.* **1994**, *98*, 6225–6230.

(22) Ohtaki, H.; Radnai, T. *Chem. Rev.* **1993**, *93*, 1157–1204.

(23) Vchirawongkwin, V.; Rode, B. M.; Persson, I. *J. Phys. Chem. B* **2007**, *111*, 4150.

(24) Julg, A. *Phys. Chem. Miner.* **1978**, *3*, 45.

(25) Hill, R. J. *Can. Mineral.* **1977**, *15*, 522.

(26) Spagnoli, D.; Kerisit, S.; Parker, S. C. *J. Cryst. Growth* **2006**, *294*, 103.

(27) Zhang, J.; Nancollas, G. H. *J. Cryst. Growth* **1990**, *106*, 181.

(28) Kowacz, M.; Putnis, C. V.; Putnis, A. *Geochim. Cosmochim. Acta* **2007**, *71*, 5168.

(29) Kerisit, S.; Parker, S. C. *J. Am. Chem. Soc.* **2004**, *126*, 10152.

(30) Higgins, S. R.; Bosbach, D.; Eggleston, C. M.; Knauss, K. G. *J. Phys. Chem. B* **2000**, *104*, 6978.

(31) Zhang, J.; Nancollas, G. H. *J. Colloid Interface Sci.* **1998**, *200*, 131.

(32) Chernov, A. A.; Petrova, E. V.; Rashkovich, L. N. *J. Cryst. Growth* **2006**, *289*, 245.

(33) Vanýsek, P. *CRC Handbook of Chemistry and Physics*; CRC Press: Cleveland, OH, 1978.

(34) Higgins, S. R.; Jordan, G.; Eggleston, C. M.; Knauss, K. G. *Langmuir* **1998**, *14*, 4967.

(35) Higgins, S. R.; Hu, X. *J. Electron Spectrosc. Relat. Phenom.* **2006**, *150*, 235.

JP8062993

DOI: 10.1021/cg901177c

CRYSTAL GROWTH & DESIGN Article
2010, Vol. 10
798–805

Self-Assembled Monolayers as Templates for Heme Crystallization

Xuefeng Wang,[†] Ellery Ingall,[†] Barry Lai,[‡] and Andrew G. Stack*[,†]

[†]*School of Earth and Atmospheric Sciences, Georgia Institute of Technology, 311 Ferst Drive, Atlanta, Georgia 30332 and* [‡]*Advanced Photon Source, Argonne National Laboratory, Argonne, Illinois, 60439*

Received September 24, 2009; Revised Manuscript Received December 2, 2009

ABSTRACT: Homogeneous self-assembled monolayers (SAMs) of alkanethiols ($HS(CH_2)_nX$) on Au(111) were used as substrates for crystallization of ferriprotoporphyrin IX (heme) in acidic aqueous solution. Different terminal functional groups (X = OH, COOH, NH_2, CH_3) were used on the SAMs as models of sites where heme crystallization takes place in blood-feeding organisms. Atomic force microscopy, X-ray diffraction (XRD), and X-ray absorption near edge spectroscopy (XANES) were employed to characterize particle morphology, density, crystallographic orientation, and the coordination environment. It was found that the morphology and extent of growth of particulates were strongly affected by the environment in which they crystallize. As has been previously observed, acicular crystals form in DMSO−methanol solution, whereas irregular aggregates of crystals form in acidic aqueous solution. Here tabular crystals were found to form on -NH_2 and -OH terminated SAMs, whereas inclined crystals formed on -COOH and -CH_3 terminated substrates. Particulate coverage on these SAMs decreased in the order of -NH_2, -COOH, -CH_3, and -OH. Chloroquine, a widely used antimalaria drug, slowed particle nucleation rate on the SAMs with varying efficacy but was most efficient on the -COOH SAM. XANES measurements showed that the coordination environment surrounding iron in the particles was found to be the same, regardless of the preparation method and matches existing spectra of hemozoin produced in vivo and synthetic β-hematin. Different crystallographic planes were found to be expressed depending on the identity of the SAM using XRD. The interaction between the terminal functional group of the SAM and the density and orientation of crystals is discussed.

1. Introduction

Hemoglobin is the main amino acid source for blood-feeding organisms. Both ingestion and degradation of hemoglobin result in a build-up of free heme, which is toxic. Crystallization of free heme as hemozoin is a major detoxification pathway in organisms such as the protozoan parasites of the genera *Plasmodium* and *Hemoproteus*, and the genus *Schistosoma* within the class Trematoda, as well as some blood-sucking arthropods.[1−4] Malaria caused by *Plasmodium falciparum* in Africa, South America, the Caribbean and Asia, and schistosomiasis caused by *Schistosoma mansoni* in Africa and Southeast Asia, are the two most prevalent tropical diseases in humans. The hemozoin synthesis pathway is the main target of antimalarial drugs comprising quinine and its derivations, and the antischistosomal effects of chloroquine reveal that hemozoin formation is also a potential target for chemotherapy in *S. mansoni*.[5,6] Thus, the study of heme crystallization will help to understand the mechanism of hemozoin formation in vivo and may yield insights that contribute to the design of effective drugs.

Hemozoin formation is a process of biologically controlled mineral formation (biomineralization). Its chemical composition and morphology are regulated to a significant degree by the organisms.[7,8,13−15] Hemozoin is chemically, spectroscopically, and crystallographically identical to β-hematin, which is synthesized in vitro.[7,8] The centrosymmetric unit cell of β-hematin is composed of a dimer of ferriprotoporphyrin IX (Fe(III)PPIX or heme), in which a propionate group of each heme molecule coordinates the central iron center of its partner. The Fe(III)PPIX dimers in the unit cell are interlinked by hydrogen bonds through a second propionic acid group (Figure 1).[8] Previous results have indicated that the shape and size of hemozoin and β-hematin crystals are dependent on their formation environment.[9−17] For example, rectangular-prism shaped hemozoin particles approximately 100 × 100 × 500 nm form in the acidic digestive vacuole of *P. falciparum*,[13] small rectangular crystals approximately 200 nm long assemble into spherical structures inside lipid droplet-like particles in *S. mansoni*, and approximately cylindrical crystallites or multicrystalline aggregates form in close association to phospholipid perimicrovillar membranes in a kissing bug *Rhodnius prolixus*.[14,15] β-Hematin synthesized in anhydrous organic solvents are acicular or elongate, rectangular wafers,[17] whereas crystals synthesized in aqueous acidic solutions form irregular aggregates.[7,17] Furthermore, the antimalarial drugs quinine and chloroquine cause the ends of β-hematin formed in methanol−DMSO or chloroform to taper.[10]

The mechanism of in vivo heme crystallization is unclear. Histine-rich protein II and III (HRP II and III) purified from the digestive vacuoles of *P. falciparum* are heme polymerases[18] and can promote hemozoin formation.[7] However, *P. vivax* and *P. berghei* lacking HRP II and III can still produce hemozoin;[19] thus, HRPs are not exclusively necessary. A novel heme detoxification protein (HDP) also mediates heme dimer formation and is functionally conserved across the *Plasmodium* genus.[20] Alternately, hydrogen bonding of the propionic acid groups of hemozoin dimers could promote crystallization in a hydrophobic lipid environment or a digestive vacuole without the aid of a dedicated polymerase.[13,14,21,22] Hemozoin formation has been detected in both intracellular vacuoles and extracellular lipid droplets, and enhanced synthetic β-hematin formation has been found in the presence of monopalmitic glycerol, monostearic glycerol,[21] and hydrophobic amino acids (leucine, isoleucine, valine, methionine, and phenylalanine).[22]

*To whom correspondence should be addressed. E-mail: andrew.stack@eas.gatech.edu.

 Published on Web 01/14/2010

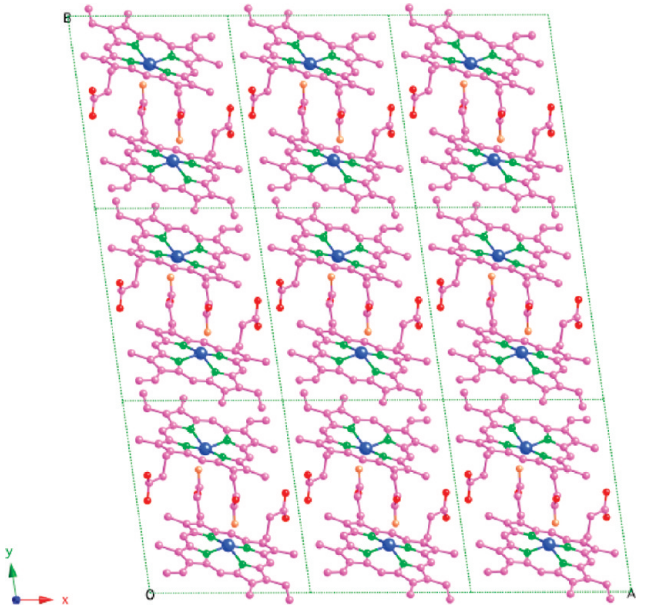

Figure 1. Crystal structure of β-hematin viewed along the [001] crystallographic axis. Fractional coordinates were obtained from ref 8. Pink circles are carbon atoms, red circles are oxygens/protons on carboxylic acid groups, orange circles are deprotonated oxygen atoms, green circles are nitrogen atoms, and blue circles are iron atoms.

Observed self-assembled heme-dimerization at the lipid/water interface also supports this hypothesis.[23] However, the inner surface of the membrane in the acidic digestive vacuole in *P. falciparum* contains polar chemical moieties such as carboxyl, amine, phosphoryl, hydroxyl, and thiol groups, and will not provide an entirely hydrophobic environment for hemozoin formation. For example, Hempelmann et al. suggest the membrane could provide favorable conditions for hemozoin formation through carboxylate groups of membrane proteins binding to the iron center of heme dimers and acting as a template for hemozoin growth.[24] Uncertainty about the digestive vacuole composition is complicated by the still unclear role of how HRPs and HDP regulate hemozoin crystal shape and size in vivo.

One method to understand how the various functional groups comprising the digestive vacuole membrane lipids and proteins affect the nucleation and growth of crystals is to create homogeneous alkanethiol self-assembled monolayers (SAMs) on gold with tunable terminal functional groups.[25] Oriented crystals of glycine,[26] L-alanine,[27] DL-valine,[27] zirconia,[28] 4-iodo-4′-nitrobiphenyl,[29] and calcite[30] have been grown on SAMs in this way previously, in addition to amorphous materials such as silica.[31] The SAMs act both as a template to stabilize nucleation clusters and to direct crystallization of these materials.[32] Here, heme crystallization was induced in acidic aqueous solution onto SAMs composed of alkanethiols with four different terminal functional groups (carboxyl, amine, hydroxyl, and methyl) in order to mimic a biomembrane. The local coordination environment around iron in heme crystals formed in the solutions and on the SAMs was examined using X-ray absorption near edge spectroscopy (XANES). The crystallographic orientation of heme crystals formed under different conditions was measured using X-ray diffraction (XRD). Lastly, nucleation and growth of heme crystals at the interface between SAMs and the saturated heme solution was examined using atomic force microscopy (AFM).

2. Experimental Section

2.1. Chemicals and Reagents. Porcine hematin, 16-mercaptohexadecanoic acid ($HS(CH_2)_{15}COOH$, 99%), 11-mercapto-1-undecanol ($HS(CH_2)_{10}CH_2OH$, 99%), 1-hexadecanethiol ($HS(CH_2)_{15}CH_3$, 99%) and 11-amino-1-undecanethiol hydrochloride ($HS(CH_2)_{10}CH_2NH_2 \cdot HCl$, 99%), propionic acid (>99.5%), 2,6-lutidine (purified by redistillation, ≥ 99%), ethanol (200 proof), methanol (99.9%), sodium hydroxide, sodium bicarbonate, and dimethyl sulfoxide (DMSO) (anhydrous, ≥ 99.9%) were used as received (Sigma-Aldrich).

2.2. Substrate Preparation. A clean silicon wafer with a 10 cm diameter (Silicon Quest International) was coated with a 10-nm-thick titanium film followed by the deposition of a 100-nm-thick gold film using an E-Beam Evaporator (CVC Products, Inc.) and diced into 1 × 1 cm squares. The small coated silicon wafers were ultrasonicated in ethanol for 10 min. SAMs of $HS(CH_2)_{10}CH_2OH$ (-OH), $HS(CH_2)_{15}COOH$ (-COOH), $HS(CH_2)_{10}CH_2NH_2$ (-NH_2), and $HS(CH_2)_{15}CH_3$ (-CH_3) were formed on gold by immersing small coated silicon wafers into a 10 mM solution of the thiol in ethanol for 48 h in an anaerobic chamber. The samples were then ultrasonicated in ethanol for 10 min.

2.3. Characterization of Substrates. The topography of SAMs and bare gold was examined using a PicoPlus AFM (Agilent Technologies). Wettability was measured by placing a drop of ultrapure water with a volume of 20 μL (≥18.2 MΩ) on each substrate and the image was recorded with a digital camera. Contact angles were measured manually.

2.4. Crystallization. Heme crystals were grown using three different methods at room temperature. The first method used was a bulk precipitation of β-hematin in acidic aqueous solution: 37.8 mg of hematin was dissolved in 8 mL of 0.1 M NaOH.[7,17] 1.828 mL of propionic acid was added dropwise while gently shaking the vessel. The flask was then sealed, protected from ambient light, and left undisturbed for four months. The precipitate was collected by centrifugation at 8000 rpm for 5 min and washed with ultrapure water three times. After the unreacted hematin in the supernatant was poured off, the precipitate was washed with 0.1 M sodium bicarbonate solution (pH = 9.1) three times, washed in ultrapure water three times, and finally dried in a vacuum oven overnight.

In the second method, SAM-covered substrates were used as described above.[30] These were suspended upside-down in a clean glass Petri dish to avoid the precipitates formed in solution from attaching to the SAMs. 14.3 mg of hematin was completely dissolved in 30.885 mL of 0.1 M NaOH, ultrasonicated for 5 min, and poured into the Petri dish. Then, 14.115 mL of propionic acid was added dropwise while shaking the dish gently, giving a final heme concentration of 0.5 mM. After being left undisturbed for 0.5 h, 2 h, 48 h and one week, the substrates were taken out, washed with ultrapure water three times, and dried in a vacuum oven overnight. The precipitate in the solution after being left for one week was treated as in the first method.

In the third method, a nonaqueous solvent was used and crystals were synthesized in the bulk.[17] All work for this method was performed in an anaerobic chamber. 69.9 mg of hematin was dissolved in 2 mL of dry 2,6-lutidine while shaking the vessel vigorously. Ten milliliters of the mixture of DMSO and methanol (V:V = 1:1) was added. The flask was sealed and placed in an anaerobic chamber for one week. The precipitate was then treated as in the first method. In order to characterize samples created using this method and the bulk aqueous method described above, the precipitate was suspended in ethanol and adsorbed onto fresh cleaved mica. The mica sample was dried in a vacuum oven overnight.

2.5. Characterization of Crystals. X-ray absorption near edge spectroscopy (XANES) of Fe in particulates formed under different conditions was performed on the X-ray Operations Research (XOR) beamline 2-ID-D at the Advanced Photon Source at Argonne National Laboratories, Illinois, USA. All measurements were conducted under a He(g) atmosphere in order to minimize absorption from, and X-ray fluorescence by low-Z elements in air, such as Ar. XANES was performed directly on the silicon wafer substrates described above. The X-ray energy scale was calibrated with standard Fe metal foil. By using a monochromator to vary the energy of the incident X-ray beam, Fe X-ray fluorescence intensity

was recorded between 7095 and 7175 eV in 0.5 eV steps using a 2-s dwell time per step. An energy dispersive Si-drift detector (Vortex EM, with a 50 mm^2 sensitive area, and a 12.5 μm Be window; SII NanoTechnology, Northridge CA, USA) was used to detect X-ray fluorescence from the sample as it was scanned over the energy range. Data was normalized against variations in the incident beam intensity by dividing the X-ray fluorescence signal by the signal obtained in an upstream ionization detector. The Fe XANES spectra were obtained by plotting the normalized X-ray fluorescence intensity versus X-ray energy. First derivatives of the XANES spectra were calculated to facilitate comparison of peak and edge positions in β-hematin standards.

The morphologies of particles grown on SAMs were examined using the AFM in an acoustic alternating current mode and the maximum scan rate was limited to 0.5 Hz in order to avoid detachment of particles with the tip. The coverage fraction, that is, the percent of the total surface area covered by particles, was estimated using image analysis software (ImageJ). Specifically, binary images were created by selecting individual particles in an AFM height image and filling contiguous portions of the particle with a solid color. Particle surface coverage percent was calculated as the ratio of the area of solid color to the total image area. For each sample, 3−5 5 × 5 μm images were analyzed.

The crystallographic planes of particles grown in aqueous solution and on the SAM and gold substrates were measured using a PANalytical X'Pert PRO Alpha-1 X-ray powder diffractometer with a 1.8 kW ceramic copper tube (λ = 1.541 Å). As a reference, a powder sample was suspended in acetone and absorbed onto a low background single-crystal Si (510) plate (Gem Dugout). Prior to imaging samples grown or deposited on substrates, the substrate, X-ray beam, and the detector were aligned into a single plane when $2\theta = 0°$. In this situation, only planes parallel to the substrate surface should produce significant diffraction intensity. Diffraction peak intensities for various crystallographic planes of β-hematin were calculated using CrystalDiffract (CrystalMaker Software Ltd.) from the β-hematin atomic structure.[8]

3. Results and Discussion

3.1. β-Hematin Growth in Solution. Nucleation was examined in solutions known to produce β-hematin in order to confirm that our growth solutions produce similar morphologies as previously established and to provide a point of comparison to growth on SAMs. In Figure 2, homogeneous acicular β-hematin crystals formed in DMSO−methanol solution, while aggregates of irregular β-hematin particles were found to form in aqueous propionic acid solution (pH = 3.16). As a point of reference, acicular β-hematin crystals also form under other conditions such as aqueous acetic acid solution mixed with methanol, ethanol, propanol, butanol, or mono-oleic glycerol.[21,33] The crystal sizes and morphologies observed in Figure 2 are consistent with previous work.

The X-ray powder diffraction pattern of crystals grown in aqueous propionic acid solution shows relatively strong peaks for the (100), (131), (031), (020), (120), ($\bar{2}$20), and (1$\bar{2}$1) planes (Figure 3). Since this is in agreement with patterns of β-hematin formed in DMSO−methanol solution[17,34] as well as hemozoin isolated from *S. mansoni* and *R. prolixus*,[14] this confirms that the method does indeed result in β-hematin crystal formation.

3.2. Self-Assembled Monolayer Characterization. XRD was used to confirm that the silicon wafer was covered in a film of gold dominantly composed of the (111) surface (Figure 4). AFM revealed that the Au film was homogeneous with a grain diameter of 53 ± 16 nm. This grain diameter is sufficiently large to allow for SAM formation and heme nucleation. The root mean squared roughness, as measured by AFM, of bare Au (111) slides was 0.7 ± 0.1 nm and similar to the roughness of the SAMs: -OH is 1.1 ± 0.1 nm, -COOH is 1.0 ± 0.1 nm, $-NH_2$ is 0.9 ± 0.1 nm, and $-CH_3$ is 0.9 ± 0.1 nm. However, the wettability of the SAMs varies substantially (Figure 5). The measured static water contact angle increases in the following sequence: -OH (29 ± 2°), -COOH (43 ± 3°), $-NH_2$ (54 ± 3°), bare Au (111) (58 ± 3°), and $-CH_3$ (93 ± 2°). The trend is qualitatively consistent with the wetting properties of the terminal groups of these SAMs on Au (111);[35] that is, the -OH surface is most hydrophilic while the $-CH_3$ surface most hydrophobic.

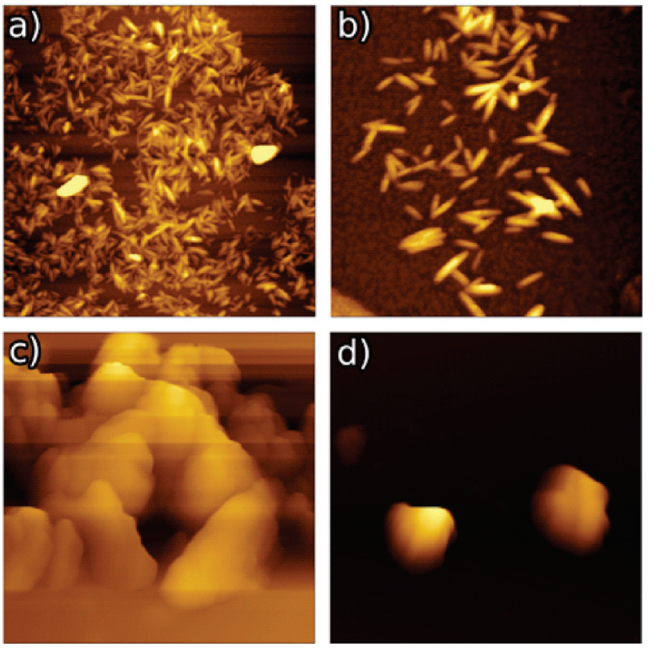

Figure 2. AFM images of β-hematin formation in DMSO−methanol solution (a, b) and aqueous propionic acid solution (c, d) for one week. The image size is 10 × 10 μm with a z-scale of 77 nm in (a), 5 × 5 μm with a z-scale of 46 nm in (b), 2 × 2 μm with a z-scale of 0.47 μm in (c), and 2 × 2 μm with a z-scale of 220 nm in (d).

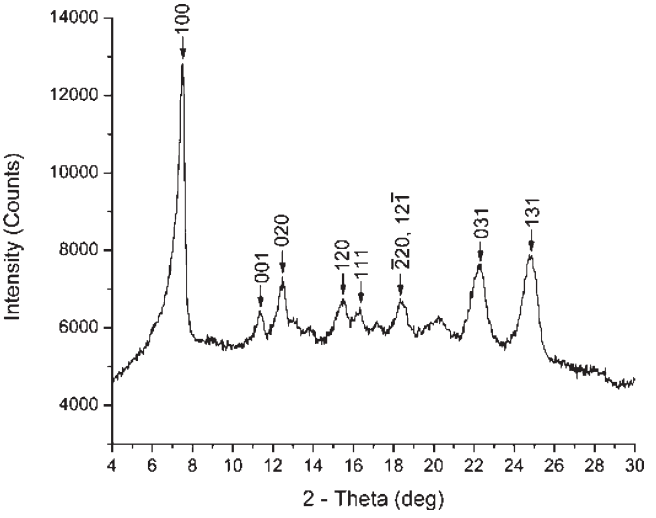

Figure 3. X-ray powder diffraction (λ = 1.542 Å) pattern of β-hematin formation in aqueous propionic solution for four months.

3.3. Nucleation and Growth of Particulates on the Self-Assembled Monolayer Surfaces. SAMs terminated with -OH, $-NH_2$, -COOH, and $-CH_3$ functional groups exposed to aqueous propionic acid growth solutions for half an hour resulted in particles with differing morphologies (Figure 6).

Particles tended to lie flat on both -OH and -NH_2 SAMs, but were thinner and longer on the latter. Particles tended to grow at an inclined angle on the -COOH and -CH_3 SAMs. However, acicular crystals form on both -OH SAM and -CH_3 SAM in anhydrous DMSO−methanol−chloroform solution,[36] which is same as the morphology of β-hematin crystals that grew in the bulk solution. It suggests that the role of the terminal functional groups on the SAMs in heme nucleation is dependent on the solvent comprising the growth solution. The property of the solvent determines the form of the solution-phase Fe(III)PPIX species, such as protic solvents (water, ethylene glycol) promote $\pi-\pi$ dimer formation, while aprotic solvents (DMSO, 2,6-lutidine) promote μ-oxo dimer formation.[37] Although β-hematin can grow in either acidic aqueous solution or DMSO, the conversion of $\pi-\pi$ dimers or μ-oxo dimers into hemozoin dimers during the crystallization process is still unknown. The differing morphology of the particles on these SAMs in propionic acid solution from those grown in aprotic solvents[36] indicates that the interaction of the terminal functional groups and soluble heme with the solvent molecules affects the crystallographic orientation of nuclei during crystal formation. While we cannot prove that the particles in Figure 6 are β-hematin, the shape and peak position in XANES spectra (Figure 7a) and first derivation of the spectra (Figure 7b) match those measured of both synthesized β-hematin in aqueous propionic acid and DMSO and in vivo produced hemozoin.[38]

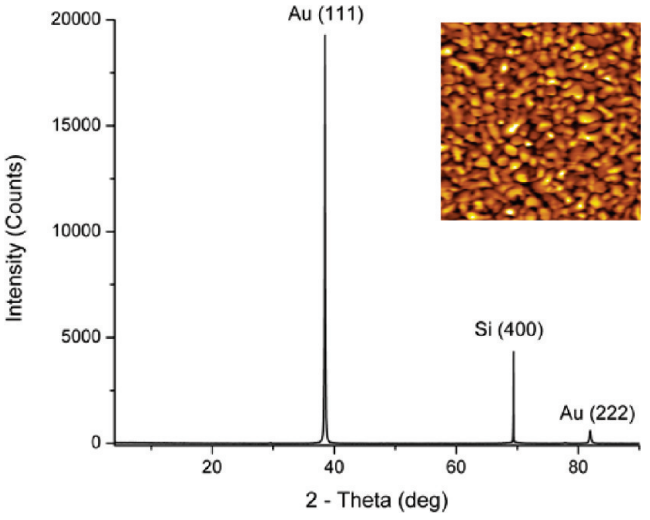

Figure 4. X-ray diffraction data of the gold thin film used as a substrate for the SAMs and an AFM image of 1 × 1 μm area with a z-scale of 10 nm.

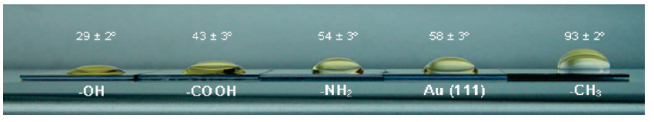

Figure 5. An optical photograph demonstrating a gradient in hydrophobicity, as measured by the contact angle of drops of ultrapure water on substrate surfaces.

The fraction of the surface covered by particles on these SAMs and mica after 0.5, 2, and 48 h was measured with AFM. Mica was chosen as the reference substrate, whose surface is flat and hydrophilic. The surface coverage fraction was lowest on mica for all three time intervals (Figure 8), which suggests that the particles adhere poorly to mica, or even form in solution and are deposited on the mica. In contrast, surface coverage on the SAMs was much higher. This suggests that the terminal functional groups of the SAMs can facilitate heme nucleation (Figure 8). The surface coverage fraction on -OH and -CH_3 SAMs for 0.5, 2, and 48 h was constant within error indicating that nucleation rate was zero. In contrast, surface coverage on the -COOH and -NH_2 SAMs continuously increased with time to completely cover the SAM with particles (Figure 8a). One explanation for the rapid saturation of nucleation on the -OH and -CH_3 SAMs is that nucleation is favorable when the heme concentration is high but as it drops due to precipitation, further nucleation rapidly becomes energetically and/or kinetically unfavorable. Nucleation and growth is likely to be much more favorable on the -COOH and -NH_2 SAMs, resulting in

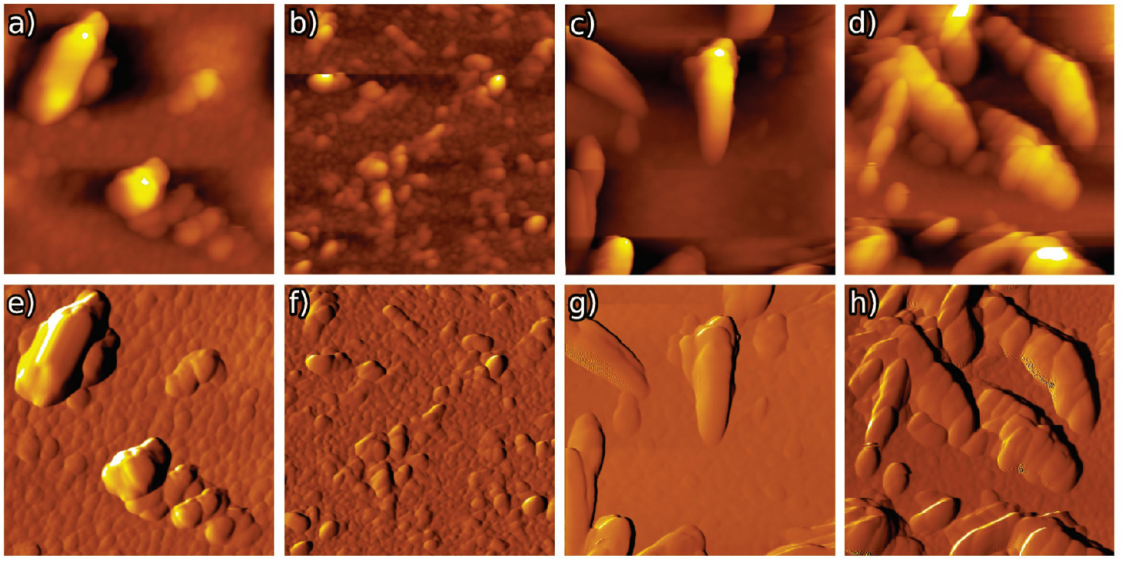

Figure 6. AFM height (a−d) and amplitude (e−h) images of particles grown for 0.5 h on (a, e) −OH, (b, f) -COOH, (c, g) -NH_2, and (d, h) -CH_3. Each image is 2 × 2 μm in size with a z-scale of 80 nm in (a and b) and 200 nm in (c and d). The amplitude scale is 1 nm in (e), 2 nm in (f), 3 nm in (g), and 4 nm in (h).

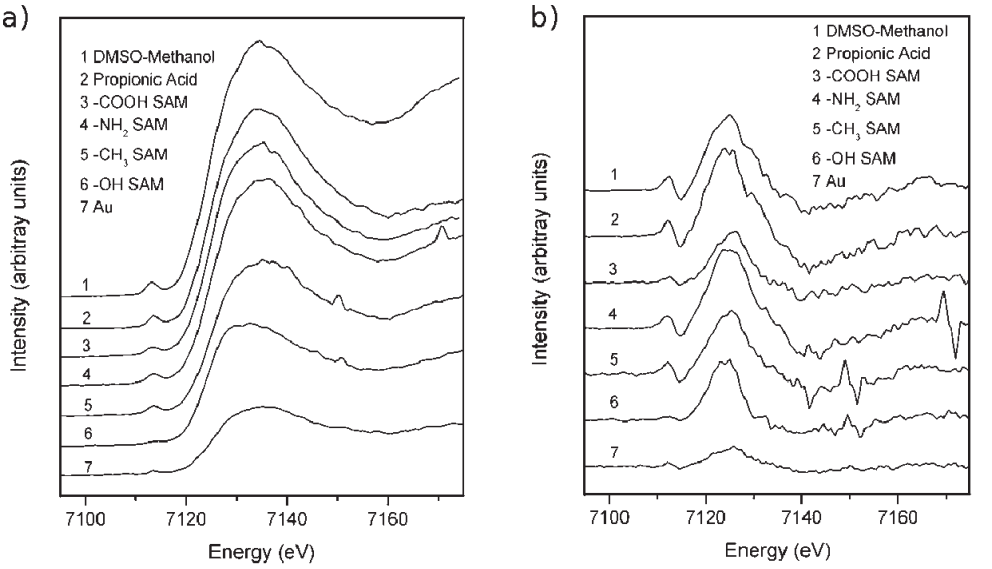

Figure 7. (a) X-ray absorption near edge spectra of Fe in heme crystals formatted in (1) anhydrous DMSO-Methanol (V:V = 1:1), (2) aqueous solution of propionic acid, (3) the -COOH SAM, (4) the -NH_2 SAM, (5) the -CH_3 SAM, and (6) the -OH SAM. 3−6 were all grown in propionic acid solution. (b) First derivatives of X-ray absorption near edge spectra in (a).

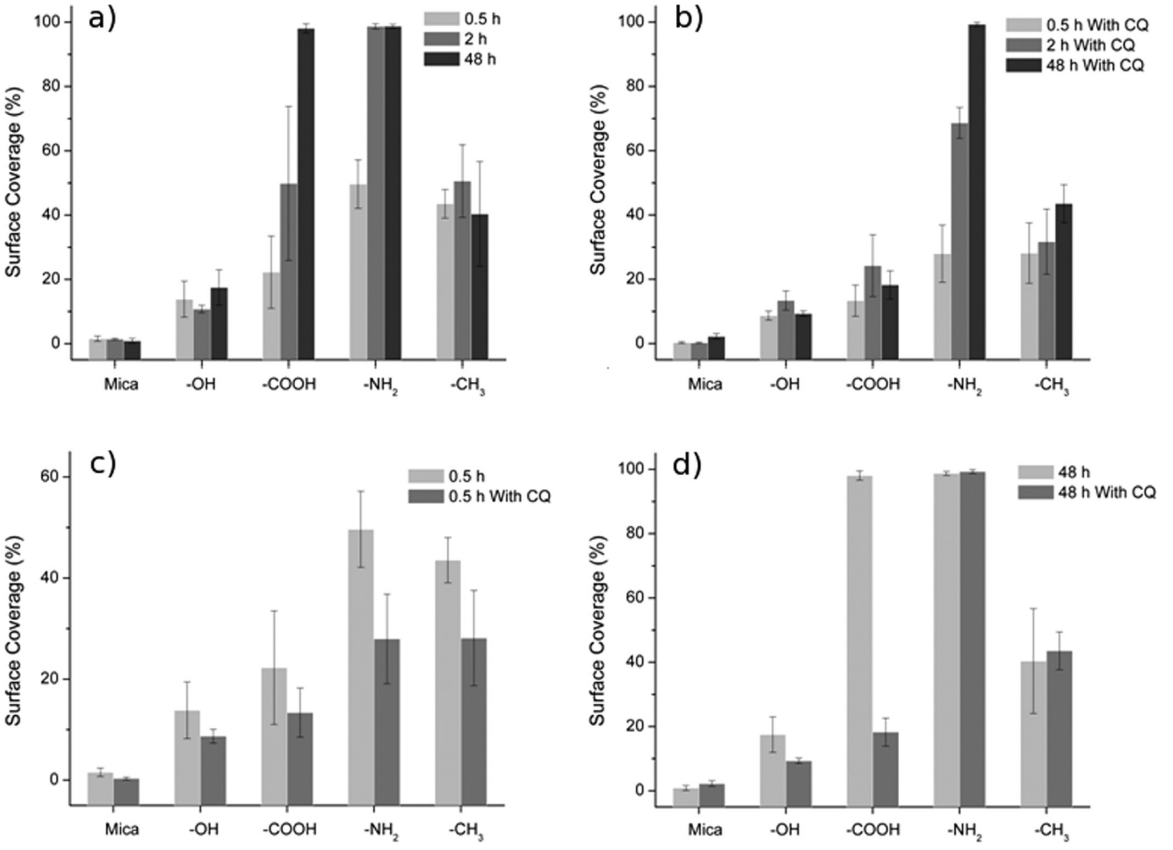

Figure 8. Particle surface coverage percent of particles grown on mica and the SAMs. (a) Growth without chloroquine as a function of time. (b) Growth with 10% chloroquine (CQ) as a function of time. (c) Growth with and without chloroquine at 0.5 h. (d) Growth with and without chloroquine at 48 h.

continuous nucleation even at lower concentrations of heme in solution. Similarly, the surface coverage of particles on the -NH_2 SAM was highest and lowest on the -OH SAM for the same duration of the experiment (Figure 8c,d).

The different nucleation behavior on these SAMs is not easily explained. In the acidic growth solution (pH = 3.16), there could be an electrostatic attraction between the protonated amine group of the -NH_2 SAM and a deprotonated carboxyl group of the hemozoin dimer.[39] However, given that the pK_a of propionic acid is 4.87, barring a substantial deviation due to the local bonding environment, any carboxyl groups on hemes exposed to solution will be protonated and only those coordinated to an iron within the dimer complex will be unprotonated. Another, more likely,

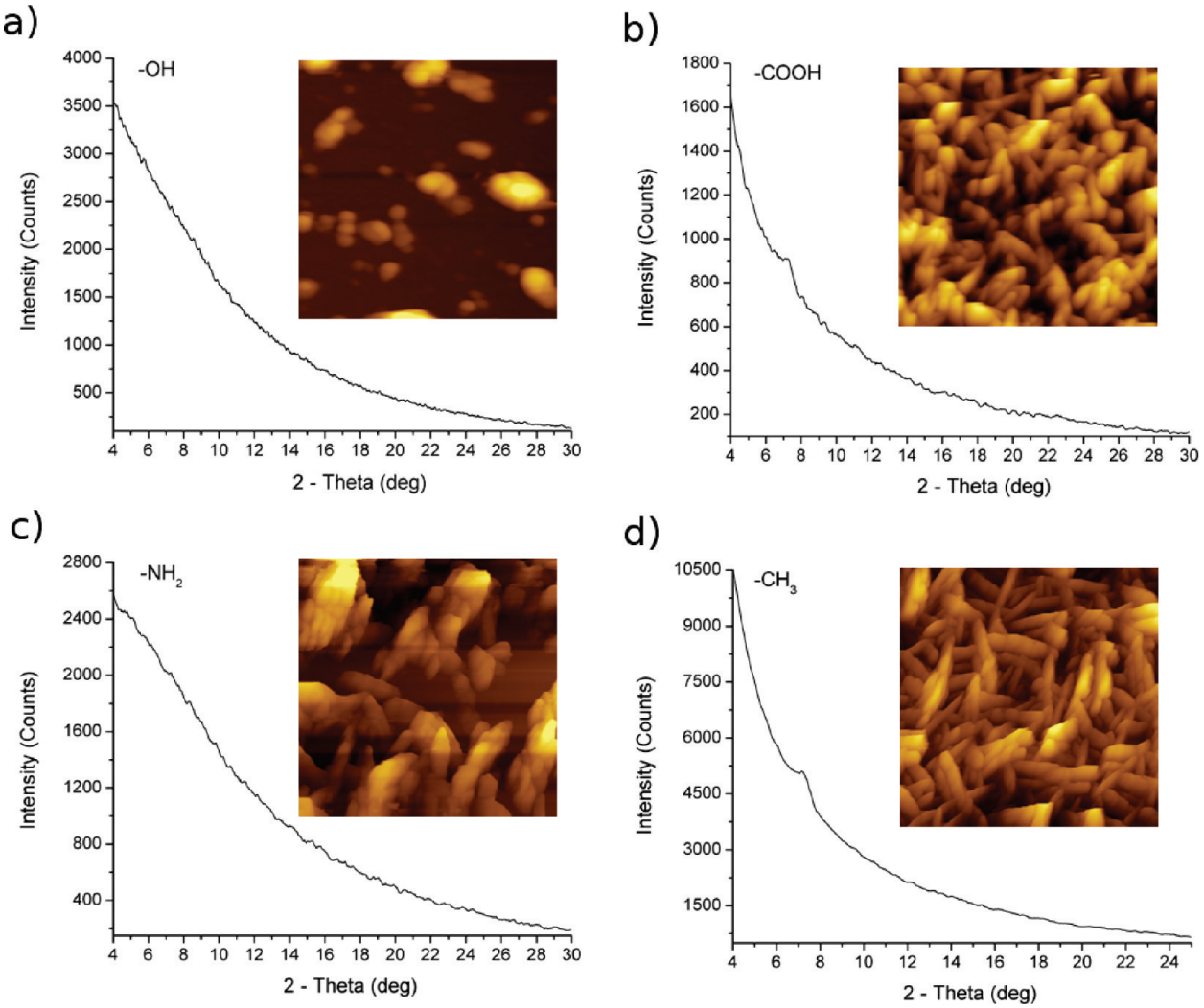

Figure 9. X-ray diffraction patterns and 5 μm × 5 μm AFM height images of β-hematin grown for one week on (a) -OH, (b) -COOH, (c) -NH_2, and (d) -CH_3. The z-scale was 156 nm in (a), 291 nm in (b), 870 nm in (c), and 400 nm in (d).

possibility is that the propionic acid groups may form hydrogen-bonded pairs with the carboxyl groups in the -COOH SAM, and single hydrogen bonds with the hydroxyl groups in the -OH SAM and the amine of the -NH_2 SAM. Finally, hydrophobic interactions may drive parts of the hemozoin dimer to adhere to the hydrophobic -CH_3 terminal functional group, although since surface coverage does not correlate with hydrophobicity of the SAMs (i.e., Figure 5), this is not expected to play a major role.

The standard antimalarial drug chloroquine was added to the growth solutions at 10% of the heme concentration to examine the drug's effect on nucleation and growth on the SAMs. Control experiments on the SAMs in the absence of heme, but in the presence of chloroquine, showed no discernible differences (data not shown). Nucleation saturated relatively quickly on mica and the -OH SAM, similar to the case without chloroquine (Figure 8b). On the -COOH SAM, however, the presence of chloroquine causes nucleation to saturate at 0.5 h as well, a dramatic contrast to the nucleation behavior in the absence of chloroquine. Additionally, all of the substrates except for the -NH_2 SAM showed a decreased particle surface coverage relative to the solutions without chloroquine at 0.5 and 48 h time intervals (Figure 8c,d). The -NH_2 SAM shows a reduced particle surface coverage at 0.5 and 2 h, but particles still completely covered the substrate after 48 h. Taken together, these results show that chloroquine slows the nucleation and growth of particles on the SAMs, but varies in the efficacy of growth inhibition depending on the terminal functional group of the SAM. Chloroquine has been shown in previous work to act as an inhibitor by binding on β-hematin surfaces to block crystal growth or by forming a chloroquine−heme dimer complex that decreases the heme dimer concentration.[12,40,41] This mechanism of interaction is likely to play a role in these experiments as well since most of the SAMs and the mica show proportionally similar decreased particle surface coverage in the presence of chloroquine. On the -COOH SAM however, the dramatic difference in the nucleation behavior suggests a further, specific interaction between the chloroquine, the SAM, and/or the soluble heme that inhibits nucleation and growth. Finally, contrary to β-hematin crystals grown in chloroform,[10] the morphology of particles grown on the SAMs in the solution with 10% chloroquine did not visibly change (data not shown). However, the morphology of the crystals grown here are probably not uniform enough to make a meaningful measurement; that is, they form irregular aggregates with or without chloroquine.

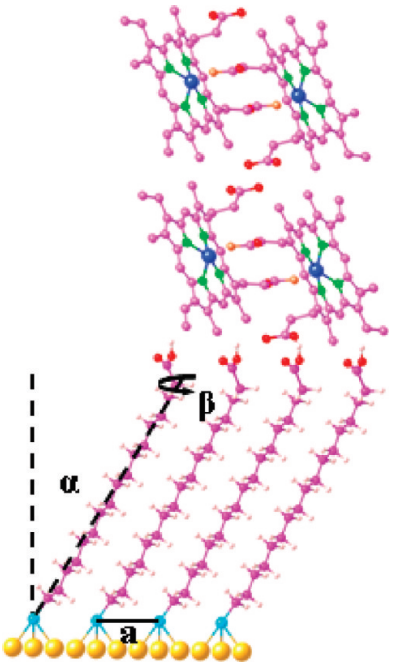

Figure 10. Schematic of a possible geometrical relationship between the unit cells of β-hematin (the upper part, the hydrogen atoms were omitted) and the structure of -COOH SAM (the lower part). A $(\sqrt{3} \times \sqrt{3})$ R30° overlayer of sulfur atoms on Au (111) with the distance between two sulfur atoms (a) of 4.984 Å. View parallel to the surface, geometry of -COOH SAM on Au (111) with the molecular cant angle (α) of 28°−40° and the twist angle (β) of 50°−55°.[42,43] Yellow circles are gold atoms, cyan circles are sulfur atoms, red circles are oxygen/hydrogen atoms on carboxylic acid groups, orange circles are deprotonated oxygen atoms, light pink circles are hydrogen atoms, dark pink circles are carbon atoms, green circles are nitrogen atoms, and blue circles are iron atoms.

The specific crystallographic orientation expressed by particles grown for one week on the SAMs varies substantially when measured with X-ray diffractometry (Figure 9). First, there was no obvious peak in the XRD spectrum of the particles grown on the -OH SAM, although particles had grown (Figure 9a). It is likely that the reason for this is that too few particles had grown to obtain a detectable diffraction intensity. On the -COOH SAM, the peak at 6.5−8.0° 2θ coincides with the location of the {100} plane reflection on β-hematin (Figure 3) and suggests that there may be a preferred orientation for the crystals grown on the SAM (Figure 9b). If the {100} is also the dominant nucleation plane, it may be that $\pi-\pi$ dimers in acidic aqueous solution absorb through hydrogen bonding between the propionate groups of the heme dimers and the carboxyl of the SAM, followed by $\pi-\pi$ dimer conversion into hemozoin dimers (orientation shown in Figure 10). In contrast, crystals grown on -COOH SAM in dry DMSO−methanol−chloroform show no preferred orientation,[36] although SAMs terminated with $-CH_3$ and -OH groups preferentially expressed the {100} face as well as the {010} in the case of the $-CH_3$. We speculate that this could be due to the relatively hydrophobic μ-oxo dimers in aprotic solvents which absorb on the SAM in a random fashion.

No peak in the XRD spectrum was observed on the $-NH_2$ SAM, although there was 100% coverage of the crystals (Figure 9c). The lack of a peak does not necessarily indicate that the precipitate is amorphous, however. Given the regular inclination of the particles grown on $-NH_2$ SAMs, we believe it is likely that the dominant nucleation plane of the crystal grown on this SAM does not diffract X-rays well, or is misaligned. The $-CH_3$ terminated SAM showed a peak in the 6.7−7.8° 2θ range likely to be the {100} reflection of β-hematin (Figure 9c), similar to particles grown on the -COOH SAM, although in this case it is not clear what interactions might be driving the crystallization. The preferred {100} or {010} nucleation face of the crystals grown on $-CH_3$ SAM in anhydrous organic solution[33] suggests that the preferred hydrophobic interaction between the methyl groups on $-CH_3$ SAM and the porphyrin ring planes in μ-oxo dimers plays a major role in inducing oriented nucleation of β-hematin.

4. Conclusions

Homogeneous SAMs of alkanethiols with hydroxyl, carboxyl, amine, and methyl terminal functional groups were deposited on Au (111) surfaces and were used as the substrates for heme crystallization in acidic aqueous solution. The identity of the terminal functional group in the SAM was found to affect the morphology, density, and orientation of crystals grown on the substrates. That is, flat or tabular particles tended to grow on the -OH and $-NH_2$ SAMs, whereas inclined particles grew on the -COOH and $-CH_3$ SAMs. Particle surface coverage density increases in the order of -OH, $-CH_3$, -COOH, $-NH_2$ terminated SAMs. XANES spectra showed the coordination environment surrounding iron in the particles grown here and β-hematin synthesized in aqueous propionic acid solution and anhydrous DMSO−methanol solution is the same. The {100} plane of β-hematin is preferentially expressed on the -COOH and $-CH_3$ SAMs, but no detectable peaks were observed for the other SAMs. Finally, chloroquine was found to slow and even inhibit the nucleation and growth of the particles on the SAMs with varying efficacy with substantial reduction in surface coverage on the -COOH SAM. These results may help us to understand the role of the inner surface of the membrane in the digestive vacuole in malaria parasite *P. falciparum* and HRPs and lipids in promoting hemozoin formation in vivo by acting as the locations to recruit the hemozoin dimers through their individual moieties such as carboxyl, amine, hydroxyl, methyl, and phosphoryl groups.

Acknowledgment. Use of the Advanced Photon Source was supported by the U.S. Department of Energy, Office of Science, Office of Basic Energy Sciences, under Contract No. DE-AC02-06CH11357. This work was supported in part by the U.S. National Science Foundation Grant 0849494 to EI and U.S. Department of Energy Grant DE-FG02-07ER15901 to A.G.S.

References

(1) Egan, T. J. *Mol. Biochem. Parasitol.* **2008**, *157*, 127–136.
(2) Chen, M. M.; Shi, L. R.; Sullivan, D. J. *Mol. Biochem. Parasitol.* **2001**, *113*, 1–8.
(3) Oliveira, M. F.; Gandara, A. C. P.; Braga, C. M. S.; Silva, J. R.; Mury, F. B.; Dansa-Petretski, M.; Menezes, D.; Vannier-Santos, M. A.; Oliveira, P. L. *Comp. Biochem. Phys. C* **2007**, *146*, 168–174.
(4) Weissbuch, I.; Leiserowitz, L. *Chem. Rev.* **2008**, *108*, 4899–4914.
(5) Ziegler, J.; Linck, R.; Wright, D. W. *Curr. Med. Chem.* **2001**, *8*, 171–189.
(6) Oliveira, M. F.; d'Avila, J. C. P.; Tempone, A. J.; Soares, J.; Rumjanek, F. D.; Ferreira-Pereira, A.; Ferreira, S. T.; Oliveira, P. L. *J. Infect. Dis.* **2004**, *190*, 843–852.
(7) Slater, A. F. G.; Swiggard, W. J.; Orton, B. R.; Flitter, W. D.; Goldberg, D. E.; Cerami, A.; Henderson, G. B. *Proc. Natl. Acad. Sci. U.S.A.* **1991**, *88*, 325–329.

(8) Pagola, S.; Stephens, P. W.; Bohle, D. S.; Kosar, A. D.; Madsen, S. K. *Nature* **2000**, *404*, 307–310.
(9) Huy, N. T.; Uyen, D. T.; Sasai, M.; Trang, D. T. X.; Shiono, T.; Harada, S.; Kamei, K. *Anal. Biochem.* **2006**, *354*, 305–307.
(10) Solomonov, I.; Osipova, M.; Feldman, Y.; Baehtz, C.; Kjaer, K.; Robinson, I. K.; Webster, G. T.; McNaughton, D.; Wood, B. R.; Weissbuch, I.; Leiserowitz, L. *J. Am. Chem. Soc.* **2007**, *129*, 2615–2627.
(11) Gligorijevic, B.; McAllister, R.; Urbach, J. S.; Roepe, P. D. *Biochemistry* **2006**, *45*, 12400–12410.
(12) Buller, R.; Peterson, M. L.; Almarsson, O.; Leiserowitz, L. *Cryst. Growth Des.* **2002**, *2*, 553–562.
(13) Noland, G. S.; Briones, N.; Sullivan, D. J. *Mol. Biochem. Parasit.* **2003**, *130*, 91–99.
(14) Oliveira, M. F.; Kycia, S. W.; Gomez, A.; Kosar, A. J.; Bohle, D. S.; Hempelmann, E.; Menezes, D.; Vannier-Santos, M. A.; Oliveira, P. L.; Ferreira, S. T. *Febs Lett.* **2005**, *579*, 6010–6016.
(15) Silva, J. R.; Mury, F. B.; Oliveira, M. F.; Oliveira, P. L.; Silva, C. P.; Dansa-Petretski, M. *Insect Biochem. Mol. Biol.* **2007**, *37*, 523–531.
(16) Pisciotta, J. M.; Ponder, E. L.; Fried, B.; Sullivan, D. *Int. J. Parasitol.* **2005**, *35*, 1037–1042.
(17) Bohle, D. S.; Kosar, A. D.; Stephens, P. W. *Acta Crystallogr. D* **2002**, *58*, 1752–1756.
(18) Sullivan, D. J.; Gluzman, I. Y.; Goldberg, D. E. *Science* **1996**, *271*, 219–222.
(19) Sullivan, D. J. *Int. J. Parasitol.* **2002**, *32*, 1645–1653.
(20) Dewal, J.; Nagarkatti, R.; Beatty, W.; Angel, R.; Slebodnick, C.; Andersen, J.; Kumar, S.; Rathore, D. *PLoS Pathog.* **2008**, *4*, 1–15.
(21) Pisciotta, J. M.; Coppens, I.; Tripathi, A. K.; Scholl, P. F.; Shuman, J.; Bajad, S.; Shulaev, V.; Sullivan, D. J. *Biochem. J.* **2007**, *402*, 197–204.
(22) Uyen, D. T.; Huy, N. T.; Trang, D. T. X.; Nhien, N. T. T.; Oida, T.; Hirayama, K.; Harada, S.; Kamei, K. *Biol. Pharm. Bull.* **2008**, *31*, 1483–1488.
(23) Egan, T. J.; Chen, J. Y. J.; de Villiers, K. A.; Mabotha, T. E.; Naidoo, K. J.; Ncokazi, K. K.; Langford, S. J.; McNaughton, D.; Pandiancherri, S.; Wood, B. R. *Febs Lett.* **2006**, *580*, 5105–5110.
(24) Hempelmann, E.; Motta, C.; Hughes, R.; Ward, S. A.; Bray, P. G. *Trends Parasitol.* **2003**, *19*, 23–26.
(25) Love, J. C.; Estroff, L. A.; Kriebel, J. K.; Nuzzo, R. G.; Whitesides, G. M. *Chem. Rev.* **2005**, *105*, 1103–1169.
(26) Kang, J. F.; Zaccaro, J.; Ulman, A.; Myerson, A. S. *Langmuir* **2000**, *16*, 3791–3796.
(27) Lee, A. Y.; Ulman, A.; Myerson, A. S. *Langmuir* **2002**, *18*, 5886–5898.
(28) Bandyopadhyay, K.; Vijayamohanan, K. *Langmuir* **1998**, *14*, 6924–6929.
(29) Hiremath, R.; Varney, S. I.; Swift, J. A. *Chem. Mater.* **2004**, *16*, 4948–4954.
(30) Aizenberg, J.; Black, A. J.; Whitesides, G. H. *J. Am. Chem. Soc.* **1999**, *121*, 4500–4509.
(31) Wallace, A. F.; De Yoreo, J. J.; Dove, P. M. *J. Am. Chem. Soc.* **2009**, *131*, 5244–5250.
(32) Pouget, E. M.; Bomans, P. H. H.; Goos, J. A. C. M.; Frederik, G. W.; Sommerdijk, N. A. J. M. *Science* **2009**, *323*, 1455–1458.
(33) Huy, N. T.; Maeda, A.; Uyen, D. T.; Trang, D. T. X.; Sasai, M.; Shiono, T.; Oida, T.; Harada, S.; Kamei, K. *Acta Trop.* **2007**, *101*, 130–138.
(34) Bohle, D. S.; Kosar, A. D.; Stephens, P. W. *Can. J. Chem.* **2003**, *81*, 1285–1291.
(35) Dubois, L. H.; Zegarski, B. R.; Nuzzo, R. G. *J. Am. Chem. Soc.* **1990**, *112*, 570–579.
(36) de Villiers, K. A.; Osipova, M.; Mabotha, T. E.; Solomonov, I.; Feldman, Y.; Kjaer, K.; Weissbuch, I.; Egan, T. J.; Leiserowitz, L. *Cryst. Growth Des.* **2009**, *9*, 626–632.
(37) Asher, C.; de Villiers, K.; Egan, T. J. *Inorg. Chem.* **2009**, *48*, 7994–8003.
(38) Karns, G. A.; Gallagher, W. A.; Elliott, W. B. *Bioorg. Chem.* **1979**, *8*, 69–81.
(39) Vezenov, D. V.; Noy, A.; Rozsnyai, L. F.; Lieber, A. M. *J. Am. Chem. Soc.* **1997**, *119*, 2006–2115.
(40) Vippagunta, S. R.; Dorn, A.; Ridley, R. G.; Vennerstrom, J. L. *Biochim. Biophys. - Gen. Subj.* **2000**, *1475*, 133–140.
(41) Walczak, M.; Lawniczak-Jablonska, K.; Sienkiewicz, A.; Demchenko, I. N.; Piskorska, E.; Chatain, G.; Bohle, D. S. *Nucl. Instrum. Methods B* **2005**, *238*, 32–38.
(42) Vericat, C.; Vela, M. E.; Salvarezza, R. C. *Phys. Chem. Chem. Phys.* **2005**, *7*, 3258–3268.
(43) Nuzzo, R. G.; Dubois, L. H.; Allara, D. L. *J. Am. Chem. Soc.* **1990**, *112*, 558–569.